Computational Geosciences (2024) 28:1–21
https://doi.org/10.1007/s10596-023-10231-4

ORIGINAL PAPER

Numerical simulation of multiscale fault systems with rate- and state-dependent friction

Carsten Gräser[1] · Ralf Kornhuber[2] · Joscha Podlesny[2]

Received: 14 February 2022 / Accepted: 9 June 2023 / Published online: 31 October 2023

Abstract
We consider the deformation of a geological structure with non-intersecting faults that can be represented by a layered system of viscoelastic bodies satisfying rate- and state-depending friction conditions along the common interfaces. We derive a mathematical model that contains classical Dieterich- and Ruina-type friction as special cases and accounts for possibly large tangential displacements. Semi-discretization in time by a Newmark scheme leads to a coupled system of nonsmooth, convex minimization problems for rate and state to be solved in each time step. Additional spatial discretization by a mortar method and piecewise constant finite elements allows for the decoupling of rate and state by a fixed point iteration and efficient algebraic solution of the rate problem by truncated nonsmooth Newton methods. Numerical experiments with a spring slider and a layered multiscale system illustrate the behavior of our model as well as the efficiency and reliability of the numerical solver.

Keywords Rate- and state-dependend friction · Multibody coupling · Mortar methods · Nonsmooth multigrid

Mathematics Subject Classification (2010) 35Q86 · 49J40 · 74S05 · 65N55 · 65K15

1 Introduction

Stress accumulation and release in geological fault networks play a crucial role in earthquake dynamics. The phenomenology of faults is ranging from subduction zones like the Nasca plate and strike-slip faults like the San Andreas fault to multiscale fault systems like the Atacama zone. Strongly varying time scales between the occurrence and duration of slip events suggest to complement experimental studies in the field (or in the lab [38]) by numerical simulations.

In the underlying mathematical description, the Dieterich-Ruina model of rate- and state-dependent friction (RSF) [40] has become a standard for the frictional behaviour along the faults [7, 35, 37]. It can be regarded as an extension of simple Tresca friction with rate- and state dependent friction coefficient $\mu = \mu(V, \theta)$ that is increasing/decreasing with increasing/decreasing sliding velocity or slip rate V involving some relaxation effect as expressed by the state θ. The variational structure of RSF has been identified and first exploited by Pipping et al. [33]

The simulation of rupture and slip events in seismic hazard analysis has quite a history (cf., e.g., [3, 8, 21, 25] and the references cited therein). Utilizing a discontinuous Galerkin (DG) scheme in space in connection with arbitrary high-order (ADER) time integration, de la Puente et al [10] developed a numerical method for the dynamic simulation of slip events. This method was later generalized to three space dimensions [29] and cast into the software package SeisSol that was successfully utilized for the simulation, e.g., of the 2016 Kaikōura earthquake cascade [45]. More recently, a different approach based on a diffuse representation of faults was first applied to subduction zones [19, 44, 46] and later extended to strike-slip faults [9]. This approach has the potential to allow for much more complicated fault systems because the faults have to be no longer resolved exactly by the underlying finite

✉ Carsten Gräser
graeser@math.fau.de

Ralf Kornhuber
kornhuber@math.fu-berlin.de

Joscha Podlesny
podlesjo@math.fu-berlin.de

1 Department Mathematik, Friedrich-Alexander-Universität Erlangen–Nürnberg, 91058 Erlangen, Germany

2 Institut für Mathematik, Freie Universität Berlin , 14195 Berlin, Germany

element mesh. However, this advantage currently comes with high computational cost due to a lack of efficient algebraic solution techniques.

In this paper, we extend a variational approach to the simulation of subduction zones [32] to a layered fault system with RSF. More precisely, we consider the deformation of a geological structure with non-intersecting faults that can be represented by I viscoelastic bodies undergoing small viscoelastic deformations and large tangential displacements with RSF contact conditions. Assuming existence of a sufficiently regular contact mapping, we formulate a general mathematical model that contains Dieterich–Ruina friction as a special case. Fault opening is forbidden for notational convenience, but could be included in a straightforward way.

Time discretization is performed by a classical Newmark scheme, resulting in a coupled system of nonsmooth, convex minimization problems that has to be solved in each time step. Decoupling this system by a fixed point iteration leads to a problem for the velocity (and thus for the rate) with given state, and an independent state problem with given rate. Both the rate and the state problem can be rewritten as convex minimization problems admitting unique solutions. For a related coupled problem with unilateral contact, as arising from the mathematical description of subduction zones, existence and uniqueness of solutions was established by Pipping et al. [30, 33] using fixed point arguments.

Spatial discretization of the rate problem is performed by a mortar method in the spirit of Krause and Wohlmuth [24, 48, 49]. This approach has the advantage that it provides nodal block separation of the nonsmooth nonlinearity which allows for direct application of globally convergent Truncated Nonsmooth Newton Multigrid (TNNMG) methods [14–16]. The state problem is discretized by piece-wise constant finite elements. For given rate, the resulting algebraic problem decouples into independent scalar problems for each of the nodal values, which can be solved, e.g., by simple bisection or even explicitly.

While both our mathematical model and our numerical solution methods are applicable in $d = 2, 3$ space dimensions, our numerical experiments are restricted to $d = 2$ for reasons of computational complexity. We consider a spring slider with $I = 2$ bodies and a layered network with $I = 5$ bodies separated by 4 faults subject to prescribed velocities at the upper boundary. We perform self-adaptive time stepping to efficiently resolve strongly varying velocities during loading, rupture, and sliding. Spatial discretization is based on triangulations as obtained by adaptive refinement concentrated at the faults. The associated hierarchy of finite element spaces is used for the algebraic TNNMG solver of the rate problems with given state as arising in the fixed point iteration mentioned above.

For the spring slider we observe the periodic occurrence of mostly unilateral slip events, similar to related simulations of subduction zones [32]. These slip events are nicely captured by adaptive time stepping, while the number of outer fixed point iterations and inner multigrid iteration remains almost the same for all time steps. Simulation of the layered network exhibits an interesting coincidence of periodic slip events along the upper fault with loading phases and oscillatory behavior on the others. We observe essentially the same efficiency of time stepping, fixed point iteration, and multigrid as for the spring slider which illustrates the robustness of our numerical solution procedure, also with respect to the number of faults.

2 Mathematical modelling

In the following section we will introduce the mathematical model for layered fault systems with multiple faults and rate- and state-dependent friction. To this end we will extend the variational approach introduced in [32] for the case of two faults. The introduced model is based on the assumption that each layer undergoes small viscoelastic deformations, while the relative tangential displacement between different layers can be large.

2.1 A layered fault system with rate- and state-dependent friction

We consider a geological structure containing a system of faults which is represented by a deformable body with reference domain $\Omega \subset \mathbb{R}^d$, $d = 2, 3$, that, along the faults, is decomposed into I subdomains Ω_i, $i = 1, \dots, I$,

$$\overline{\Omega} = \bigcup_{i=1}^{I} \overline{\Omega}_i.$$

We assume that these subdomains are non-empty, bounded Lipschitz domains, do not penetrate each other and are layered in the sense that at most two subdomains are in contact at any point in $\mathbb{R}^d$ (see Fig. 1).

Then, the subdomains can be ordered such that there is a common interface $\Gamma^F_{i,i+1} = \overline{\Omega}_i \cap \overline{\Omega}_{i+1}$, $i = 1, \dots, I-1$, and all other intersections of subdomains are empty. Setting $\Gamma^F_{0,1} = \Gamma^F_{I,I+1} = \emptyset$ for notational convenience, the boundary $\partial\Omega_i$ of Ω_i is disjointly decomposed according to $\partial\Omega_i = \Gamma^D_i \cup \Gamma^N_i \cup (\Gamma^F_{i-1,i} \cup \Gamma^F_{i,i+1})$, into a Dirichlet, a Neumann, and a contact boundary, respectively. We set

$$\Gamma^D = \bigcup_{i=1}^{I} \Gamma^D_i, \quad \Gamma^N = \bigcup_{i=1}^{I} \Gamma^N_i, \quad \Gamma^F = \bigcup_{i=1}^{I-1} \Gamma^F_{i,i+1}.$$

For $v = (v_1, \dots, v_I)$ with $v_i : \Omega_i \to \mathbb{R}^d$, $i = 1, \dots, I$, we define the restrictions $v_T = (v_{T,1}, \dots, v_{T,I-1})$ and

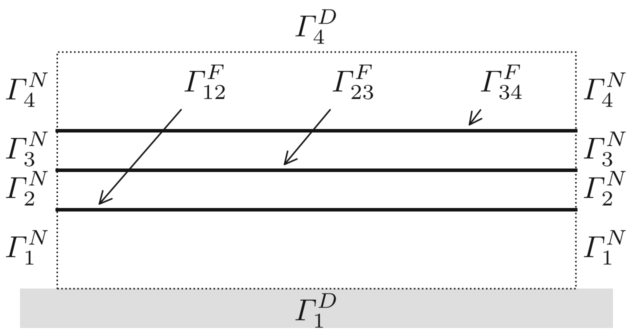

Fig. 1 A fault system Γ^F with $I = 4$ subdomains and $I - 1 = 3$ layered faults

$v_B = (v_{B,1}, \ldots, v_{B,I-1})$ of v to Γ^F with

$$v_{T,i} = v_{i+1}|_{\Gamma^F_{i,i+1}}, \quad v_{B,i} = v_i|_{\Gamma^F_{i,i+1}} \qquad i = 1, \ldots, I-1,$$

denoting the restrictions from the top Ω_{i+1} and the bottom Ω_i, respectively (see Fig. 1). It is convenient to identify $v_T = (v_{T,1}, \ldots, v_{T,I-1})$ and $v_B = (v_{B,1}, \ldots, v_{B,I-1})$ with functions v_T and v_B defined on Γ^F by $v_T|_{\Gamma^F_{i,i+1}} = v_{T,i}$ and $v_B|_{\Gamma^F_{i,i+1}} = v_{B,i}$, $i = 1, \ldots, I-1$. Let $n = (n_1, \ldots, n_I)$ where $n_i \in \mathbb{R}^d$ stands for the outer normal to Ω_i, $i = 1, \ldots I$. Note that n_i is an inward normal to Ω_{i+1} on $\Gamma^F_{i,i+1}$. In particular, $n_T = (n_{T,1}, \ldots, n_{T,I-1})$ and $n_B = -n_T$ are top and bottom normals on Γ^F, respectively. In the following, most quantities will be defined in terms of the bottom side.

We suppose that a body force f acts on all of Ω and surface forces f^N act on the Neumann boundary Γ^N. On the Dirichlet boundary Γ^D the velocity $\dot{u}(t)$ of the displacement field $u(t)$ of the deformable body Ω is fixed at all time instants $t > 0$. We set $u(t) = \dot{u}(t) = 0$ on Γ^D for convenience, though all further considerations can be generalized to the case of inhomogeneous boundary conditions in a straightforward way.

We assume that the boundary forces are compressive in the sense that no fault opening occurs. This means that neighboring bodies Ω_i and Ω_{i+1}, $i = 1, \ldots, I-1$, remain in contact throughout the evolution.

We consider a deformation field

$$u = (u_1, \ldots, u_I) \in H^1(\Omega_1)^d \times \cdots \times H^1(\Omega_I)^d$$

where u_i is the deformation of the subdomain Ω_i. Throughout the paper we assume that the deformations u_i within each subdomain Ω_i are small, while the relative displacement between different subdomains can be large. Thus we will use a (geometrically) linear elastic approach inside of the subdomains Ω_i while the coupling conditions have to take care of potentially large deformations.

Large deformation coupling conditions will be defined in terms of the deformed subdomains. Given the deformation fields u_i the associated displacements are given by $\mathrm{Id} + u_i$ leading to the deformed subdomains $(\mathrm{Id} + u_i)(\Omega_i)$. The actual contact surface of the deformed subdomains is then given by $\mathcal{C}^u = (\mathrm{Id} + u_B)(\Gamma^F) \cap (\mathrm{Id} + u_T)(\Gamma^F)$. In the following, we assume that each $\mathrm{Id} + u_i$ is injective, i.e. that each u_i is regular enough to avoid self-penetration of Ω_i. Furthermore, we assume that deformations are small, such that different surfaces $\Gamma^F_{i,i+1}$ do not get in contact after deformation. Then, the deformed contact boundary can be pulled back to the bottom and top reference domain according to

$$\Gamma^{F,u}_B = (\mathrm{Id} + u_B)^{-1}(\mathcal{C}^u) \subset \Gamma^F,$$
$$\Gamma^{F,u}_T = (\mathrm{Id} + u_T)^{-1}(\mathcal{C}^u) \subset \Gamma^F.$$

In the following, we will parameterize the top reference domain $\Gamma^{F,u}_T$ over the bottom one $\Gamma^{F,u}_B$ by the bijective contact mapping

$$\pi^u : \Gamma^{F,u}_B \to \Gamma^{F,u}_T, \qquad \pi^u = (\mathrm{Id} + u_T)^{-1} \circ (\mathrm{Id} + u_B),$$

which maps each bottom point $x \in \Gamma^{F,u}_B$ to the unique top point $y \in \Gamma^{F,u}_T$, such that the corresponding displaced points $(\mathrm{Id} + u_B)(x)$ and $(\mathrm{Id} + u_T)(y)$ coincide. As a consequence, the deformed contact boundary $\mathcal{C}^u$ can be parametrized both over $\Gamma^{F,u}_B$ using $\mathrm{Id} + u_B = (\mathrm{Id} + u_T) \circ \pi^u$ and over $\Gamma^{F,u}_T$ using $\mathrm{Id} + u_T = (\mathrm{Id} + u_B) \circ (\pi^u)^{-1}$.

Now, consider any piecewise defined scalar or vector field

$$v = (v_1, \ldots, v_I) \in H^1(\Omega_1)^k \times \cdots \times H^1(\Omega_I)^k$$

with $k = 1$ or $k = d$. Then, we define the jump of v across the deformed contact boundary $\mathcal{C}^u$ on the contact reference domain $\Gamma^{F,u}_B$ according to

$$[v]^u = v_B - v_T \circ \pi^u \qquad \text{on } \Gamma^{F,u}_B. \tag{1}$$

Contact conditions and friction laws will be stated in terms of normal and tangential components on the deformed contact boundary $\mathcal{C}^u$. To this end, let $i = 1, \ldots I$ and denote by $n^u(x)$ an outer normal to $(\mathrm{Id} + u_i)(\Omega_i)$ at the point $(\mathrm{Id} + u_i)(x)$, $x \in \Gamma^F_{i,i+1} \cap \Gamma^{F,u}_B$, i.e. n^u is the pullback of an oriented normal field of the deformed contact boundary $\mathcal{C}^u = (\mathrm{Id} + u_B)(\Gamma^{F,u}_B)$ to $\Gamma^{F,u}_B$ using the map $\mathrm{Id} + u_B$. Then we can decompose any vector field on $\Gamma^{F,u}_B$ according to its normal and tangential components with respect to the deformed configuration as

$$v = v_t + v_n n^u, \qquad v_n = v \cdot n^u, \qquad v_t = v - v_n n^u.$$

It is important to note that the tangential and normal component are defined in terms of the u-dependent normal field n^u

that is defined (piecewise) on the deformed bottom subdomains $(\mathrm{Id} + u_i)(\Omega_i)$ and not with respect to the normal field of the reference subdomains Ω_i.

We state a closed-fault condition (no penetration and no fault opening) by prescribing that the relative motion of the deformed subdomains Ω_i and Ω_{i+1} is tangential to the actual contact surface $\mathcal{C}^u$, i.e.

$$0 = [\dot{u}]^n \cdot n^u. \tag{2}$$

As a consequence, the jump of the relative tangential velocity satisfies

$$[\dot{u}]^n_t = [\dot{u}]^n - ([\dot{u}]^n \cdot n^u) n^u = [\dot{u}]^n \quad \text{on } \Gamma_B^{F,u}.$$

The closed-fault condition is complemented by the balance of normal forces

$$(\boldsymbol{\sigma}(u)n)_B = -\omega^u (\boldsymbol{\sigma}(u)n)_T \circ \pi^u \tag{3}$$

on $\Gamma_B^{F,u}$, where $\boldsymbol{\sigma}(u)$ denotes the stress tensor on Ω. Note that the normal force $(\boldsymbol{\sigma}(u)n)_T$ is a force per surface area, such that the change of the area element induced by the pullback to $\Gamma_B^{F,u}$ using π^u has to be compensated by the weighting factor $\omega^u = \sqrt{\det((D\pi^u)^T D\pi^u + n_B \otimes n_B)}$, while the minus sign compensates for the change of the normal direction on opposing sides. Note that the balance of normal forces Eq. 3 can alternatively be phrased as a jump condition with a transformed weighting factor $\omega^u \circ (\pi^u)^{-1}$.

Utilizing $[\dot{u}]^u_t = [\dot{u}]^u$, we prescribe a rate- and state-dependent friction law of the form

$$-\sigma_t \in \partial_{[\dot{u}]^u} \phi([\dot{u}]^u, \alpha) \quad \text{on } \Gamma_B^{F,u}. \tag{4}$$

Here, we used the decomposition $(\boldsymbol{\sigma}(u)n)_B = \sigma_t + \sigma_n n^u$ of the stress field $(\boldsymbol{\sigma}(u)n)_B$ on the bottom side into its normal and tangential components

$$\begin{aligned} \sigma_n &= \boldsymbol{\sigma}_n(u) = (\boldsymbol{\sigma}(u)n)_B \cdot n^u, \\ \sigma_t &= \sigma_t(u) = (\sigma(u)n)_B - \sigma(u) n^u, \end{aligned}$$

respectively, and $\partial_{[\dot{u}]^u} \phi([\dot{u}]^u, \alpha)$ denotes the subdifferential of a state-dependent convex functional $\phi(\cdot, \alpha)$ to be described below. Note that the stress vector $(\boldsymbol{\sigma}(u)n)_B$ is computed with respect to the reference normal n_B, while its decomposition in tangential and normal components is computed with respect to the deformed configuration with the corresponding normal n^u. This reflects the fact that we assume small deformations within the subdomains while the relative deformations of subdomains can be large.

For given relative slip rate $|[\dot{u}]^u|$, the evolution of the state α is given by

$$\begin{aligned} -\dot{\alpha} &= \partial_\alpha \psi(\alpha, |[\dot{u}]^u|) \quad \text{on } \Gamma_B^{F,u}, \\ -\dot{\alpha} &= 0 \quad \text{on } \Gamma^F \setminus \Gamma_B^{F,u} \end{aligned} \tag{5}$$

with a second convex functional $\psi(\cdot, |[\dot{u}]^u|)$. Note that the state α remains constant on $\Gamma^F \setminus \Gamma_B^{F,u}$ where no contact occurs.

Assuming a visco–elastic Kelvin–Voigt material law, and fixing some final time $T_0 > 0$, we are now ready to state the following formal description of the deformation of a body Ω with a layered fault system Γ^F and rate- and state-dependent friction.

Problem 1 (Layered fault system with rate- and state dependent friction) Find

$$u\colon\ \Omega \times [0, T_0] \to \mathbb{R}^d \quad \text{and} \quad \alpha\colon\ \Gamma^F \times [0, T_0] \to \mathbb{R}$$

such that

$$\boldsymbol{\sigma}(u) = \boldsymbol{A}\boldsymbol{\varepsilon}(\dot{u}) + \boldsymbol{B}\boldsymbol{\varepsilon}(u) \quad \text{in } \Omega \setminus \Gamma^F \quad \text{(Kelvin–Voigt material)} \tag{6}$$

$$\operatorname{div} \boldsymbol{\sigma}(u) + f = \rho \ddot{u} \quad \text{in } \Omega \setminus \Gamma^F \quad \text{(balance of momentum)} \tag{7}$$

with boundary conditions,

$$\begin{aligned} u = \dot{u} &= 0 && \text{on } \Gamma^D && \text{(Dirichlet condition)} \\ \boldsymbol{\sigma}(u)n &= f^N && \text{on } \Gamma^N && \text{(Neumann condition)} \end{aligned}$$

frictional contact conditions,

$$[u]^u \cdot n^u = 0 \quad \text{on } \Gamma_B^{F,u} \quad \text{(closed-fault condition)} \tag{8}$$

$$(\boldsymbol{\sigma}(u)n)_B = -\omega^u (\boldsymbol{\sigma}(u)n)_T \circ \pi^u \quad \text{on } \Gamma_B^{F,u} \quad \text{(balance of normal forces)} \tag{9}$$

$$-\sigma_t \in \partial_{[\dot{u}]^u} \phi([\dot{u}]^u, \alpha) \quad \text{on } \Gamma_B^{F,u} \quad \text{(state-dependent friction law)} \tag{10}$$

contact state condition,

$$-\dot{\alpha} \in \partial_\alpha \psi(\alpha, |[\dot{u}]^u|), \quad \text{on } \Gamma_B^{F,u} \quad \text{(rate-dependent state law)} \tag{11}$$

and non-contact interface conditions

$$-\dot{\alpha} = 0 \quad \text{on } \Gamma^F \setminus \Gamma_B^{F,u} \quad \text{(non-contact state condition)} \tag{12}$$

$$(\boldsymbol{\sigma}(u)n)_B = 0 \quad \text{on } \Gamma^F \setminus \Gamma_B^{F,u} \quad \text{(bottom Neumann condition)} \tag{13}$$

$$(\boldsymbol{\sigma}(u)n)_T = 0 \quad \text{on } \Gamma^F \setminus \Gamma_T^{F,u} \quad \text{(top Neumann condition)} \tag{14}$$

holds for all $t \in [0, T_0]$. Here, $\rho > 0$ is a constant material density, $\boldsymbol{A}$ and $\boldsymbol{B}$ stand for the viscosity and elasticity tensor, respectively, and $\boldsymbol{\varepsilon}(v) = \frac{1}{2}(\nabla v + (\nabla v)^T)$ is the linearized strain or strain rate tensor. In addition, we impose initial conditions on the displacement u, velocity $\dot{u}$, and state α.

Throughout the following, we assume that the tensor fields $\boldsymbol{A}$ und $\boldsymbol{B}$ have the symmetry properties

$$
\begin{aligned}
\boldsymbol{A}_{ijkl} &= \boldsymbol{A}_{klij}, \qquad & \boldsymbol{A}_{ijkl} &= \boldsymbol{A}_{jikl},\\
\boldsymbol{B}_{ijkl} &= \boldsymbol{B}_{klij}, \qquad & \boldsymbol{B}_{ijkl} &= \boldsymbol{B}_{jikl}
\end{aligned}
$$

such that the stress tensor $\boldsymbol{\sigma}(u)$ and the bilinear forms induced by $\boldsymbol{A}$ and $\boldsymbol{B}$ are symmetric.

Note that Problem 1 provides an extension of the model presented in [33] that describes unilateral frictional contact of a deformable body with a rigid foundation. The tangential velocity relative to the fixed rigid foundation appearing in [33] is now replaced by the relative tangential velocity of adjacent deformable bodies.

A further extension to fault opening can be performed by replacing Eq. 8 by the non-penetration condition $[u]^u \cdot n^u \leq 0$ together with dynamical freezing and thawing of rate- and state-dependent friction Eqs. 10, 11 in case of opening or closing faults.

For ease of notation we will skip the superscript and mostly write $[\cdot] = [\cdot]^u$ in the sequel.

2.2 The Dieterich–Ruina model

The current form of the Dieterich–Ruina model of rate- and state-dependent friction goes back to [40] (see also [1, 6, 11, 27, 36, 43] and the papers cited therein). It is based on the following ansatz for the friction coefficient

$$\mu^*(V,\theta) = \mu_0 + a\log\left(\frac{V}{V_0}\right) + b\log\left(\frac{V_0\theta}{L}\right) \tag{15}$$

that depends on the rate $V = |[\dot{u}]|$ and involves positive parameters μ_0, V_0 a, b, and L.

It is complemented by a suitable evolution of the state $\theta > 0$. Here, most popular choices are

$$\dot{\theta} = 1 - \frac{V}{L}\theta \qquad \text{(Dieterich's law)} \tag{16}$$

and

$$\dot{\theta} = -\frac{V}{L}\theta\log\left(\frac{V}{L}\theta\right) \qquad \text{(Ruina's law).} \tag{17}$$

Following [33], we briefly sketch how this completely phenomenological friction model translates into a corresponding state-dependent friction law Eq. 10 and a rate-dependent state evolution Eq. 11 as postulated above. Starting from collinearity of relative tangential velocity and stress

$$-\sigma_t|[\dot{u}]| = [\dot{u}]|\sigma_t|,$$

we postulate the state equation $|\sigma_t| = \mu^*(V,\theta)|\sigma_n|$ with normal stress $\sigma_n = \sigma_n(u)$ to obtain

$$-\sigma_t = |\sigma_n|\mu^*(V,\theta)\frac{[\dot{u}]}{|[\dot{u}]|}. \tag{18}$$

In analogy to Tresca friction, we now replace the solution dependent normal stress $|\sigma_n| = |\sigma_n(u)|$ by a given parameter $|\bar{\sigma}_n|$ [33].

As $\mu^*(V,\theta)$ becomes negative and thus meaningless for

$$0 \leq V < V_m(\theta) = V_0\exp\left(-\frac{\mu_0 + b + \log(\theta V_0/L)}{a}\right)$$

we replace $\mu^*(V,\theta)$ by its regularization

$$\mu(V,\theta) = \begin{cases} \mu^*(V,\theta) & \text{if } V \geq V_m(\theta) \\ 0 & \text{otherwise} \end{cases}.$$

Then elementary calculations show that Eq. 18 takes the form Eq. 10 with the convex functional $\phi^*(\cdot,\theta) : \mathbb{R}^d \to \mathbb{R}$ defined by

$$\phi^*(v,\theta) = \begin{cases} a|\bar{\sigma}_n|\left(|v|\log(\frac{|v|}{V_m(\theta)}) - |v| + V_m(\theta)\right) & \text{if } |v| \geq V_m(\theta) \\ 0 & \text{otherwise} \end{cases}. \tag{19}$$

It remains to show that the rate evolutions Eqs. 16 and 17 can be rewritten according to Eq. 11. Introducing the transformed state $\alpha = \log\theta$, Dieterich's law Eq. 16 takes the form Eq. 11 with the scalar convex function

$$\psi_{\text{Dieterich}}(\alpha, V) = \frac{V}{L}\alpha + e^{-\alpha}. \tag{20}$$

Ruina's law Eq. 17 is recovered in terms of Eq. 11 by the same transformation and the scalar convex function

$$\psi_{\text{Ruina}}(\alpha, V) = \frac{V}{L}\left(\frac{1}{2}\alpha^2 + \log(V/L)\alpha\right). \tag{21}$$

Inserting the transformed state $\theta = e^\alpha$ into Eq. 19, we obtain the corresponding rate functional

$$\phi(\cdot,\alpha) = \phi^*(\cdot, e^\alpha). \tag{22}$$

2.3 Weak formulation

We consider the Hilbert space $H = H^1(\Omega_1)^d \times \cdots \times H^1(\Omega_I)^d$ with the canonical inner product $(v,w)_H = \sum_{i=1}^I (v_i,w_i)_{H^1(\Omega_i)^d}$, $v_i, w_i \in H^1(\Omega_i)$, $i = 1,\dots,I$, and introduce the closed linear subspace

$$H_0 = \{v \in H \mid v = 0 \text{ on } \Gamma^D\}$$

of admissible displacements respecting the Dirichlet boundary conditions. The normal jump condition is incorporated in the closed affine subspace

$$H_0^u = \{v \in H_0 \,|\, [v]^u \cdot n^u = 0\}. \tag{23}$$

With the tensors $\boldsymbol{A}$, $\boldsymbol{B}$ taken from Eq. 6, we introduce the bilinear forms

$$\begin{aligned} a(v,w) &= \int_{\Omega\setminus\Gamma^F} \boldsymbol{A}\boldsymbol{\varepsilon}(v) : \boldsymbol{\varepsilon}(w)\,dx,\\ b(v,w) &= \int_{\Omega\setminus\Gamma^F} \boldsymbol{B}\boldsymbol{\varepsilon}(v) : \boldsymbol{\varepsilon}(w)\,dx, \qquad v,w \in H_0, \end{aligned} \tag{24}$$

involving the linear strain tensor $\boldsymbol{\varepsilon}(v) = \frac{1}{2}(\nabla v + (\nabla v)^T)$, together with the linear functional

$$\ell(v) = \int_\Omega f v\,dx + \int_{\Gamma^N} f^N v\,ds, \qquad v \in H_0. \tag{25}$$

To ensure that the bilinear forms are well defined, we assume that the tensor fields $\boldsymbol{A}$ und $\boldsymbol{B}$ are uniformly elliptic in the sense that the bilinear forms induced by $\boldsymbol{A}(x)$ and $\boldsymbol{B}(x)$ on the space of symmetric $d \times d$ matrices are elliptic with constants independent of $x \in \Omega$.

By inserting the stress–strain relation Eq. 6 into the balance of momentum Eq. 7, testing with $v - \dot{u}$, integrating by parts, and exploiting the symmetry of $\boldsymbol{\sigma}(u)$ together with the boundary conditions on Γ^D and Γ^N we then formally obtain

$$\begin{aligned} \langle \rho\ddot{u}, v-\dot{u}\rangle + a(\dot{u}, v-\dot{u}) + b(u, v-\dot{u}) - \ell(v-\dot{u}) &\\ = \int_{\Gamma^F} (\boldsymbol{\sigma}(u)n)_B \cdot (v-\dot{u})_B\,ds &\\ + \int_{\Gamma^F} (\boldsymbol{\sigma}(u)n)_T \cdot (v-\dot{u})_T\,ds & \end{aligned} \tag{26}$$

for all $v \in H_0$ and $t \in (0, T_0)$. Here $\langle\cdot,\cdot\rangle$ stands for the pairing of H_0 with its dual H_0^*. Using the boundary conditions Eqs. 13 and 14, integral transformation from $\Gamma_T^{F,u}$ to $\Gamma_B^{F,u}$, and the normal force balance Eq. 9 we can rewrite the right hand side in Eq. 26 as

$$\begin{aligned} &\int_{\Gamma_B^{F,u}} (\boldsymbol{\sigma}(u)n)_B \cdot (v-\dot{u})_B\,ds + \int_{\Gamma_T^{F,u}} (\boldsymbol{\sigma}(u)n)_T \cdot (v-\dot{u})_T\,ds\\ &= \int_{\Gamma_B^{F,u}} (\boldsymbol{\sigma}(u)n)_B \cdot \Big([v-\dot{u}]^u + (v-\dot{u})_T \circ \pi^u\Big)\,ds\\ &\quad + \int_{\Gamma_B^{F,u}} \omega^u\Big((\boldsymbol{\sigma}(u)n)_T \cdot (v-\dot{u})_T\Big) \circ \pi^u\,ds\\ &= \int_{\Gamma_B^{F,u}} (\boldsymbol{\sigma}(u)n)_B \cdot [v-\dot{u}]^u\,ds. \end{aligned}$$

For given state α, we introduce the convex functional Φ^u on H_0 according to

$$\Phi^u(\cdot,\alpha) = \int_{\Gamma_B^{F,u}} \phi([\cdot]^u, \alpha)\,ds \tag{27}$$

with the convex functional ϕ taken from the friction law Eq. 10. Now let v satisfy the closed-fault condition Eq. 8, i.e. $v \in H_0^u \subset H_0$. Then, utilizing the decomposition $(\boldsymbol{\sigma}(u)n)_B = \sigma_t + \sigma_n n^u$ together with the friction law Eq. 10, the closed-fault condition $[v-\dot{u}]^u \cdot n^u = 0$ on $\Gamma_B^{F,u}$, and the definition of subdifferentials, we find that

$$\int_{\Gamma_B^{F,u}} (\boldsymbol{\sigma}(u)n)_B \cdot [v-\dot{u}]^u\,ds \ge \Phi^u(\dot{u},\alpha) - \Phi^u(v,\alpha). \tag{28}$$

Now we insert Eq. 28 into Eq. 26, in order to obtain the desired weak form of the rate equation

$$\begin{aligned} &\langle \rho\ddot{u}, v-\dot{u}\rangle + a(\dot{u}, v-\dot{u}) + b(u, v-\dot{u}) + \Phi^u(v,\alpha) - \Phi^u(\dot{u},\alpha)\\ &\quad \ge \ell(v-\dot{u}) \quad \forall v \in H_0^u. \end{aligned} \tag{29}$$

Similarly, for given velocity $\dot{u} \in H_0^u$ and thus given rate $|[\dot{u}]^u|$, we define the convex functional Ψ^u on $L^2(\Gamma^F)$ by

$$\Psi^u(\cdot,\dot{u}) = \int_{\Gamma_B^{F,u}} \psi(\cdot, \big|[\dot{u}]^u\big|)\,ds \tag{30}$$

with the convex functional ψ taken from the state law Eq. 11, and test the state evolution Eq. 11 with $\beta \in L^2(\Gamma^F)$ to obtain the weak formulation

$$(\dot{\alpha}, \beta-\alpha)_{L^2(\Gamma^F)} + \Psi^u(\beta,\dot{u}) - \Psi^u(\alpha,\dot{u}) \ge 0 \quad \forall \beta \in L^2(\Gamma^F). \tag{31}$$

This formulation automatically satisfies the non-evolution condition Eq. 12 for the state α on the non-contact boundary $\Gamma^F \setminus \Gamma^{F,u}$ since Ψ^u is defined on $L^2(\Gamma^F)$ but only depends on values of α on the contact boundary $\Gamma^{F,u}$.

We are now ready to state the weak formulation of Problem 1

Problem 2 (Weak formulation) Find

$u \in H^1((0,T_0),H_0) \cap H^2((0,T_0),H_0^*)$ and
$\alpha \in H^1((0,T_0),L^2(\Gamma^F))$

such that $\dot{u} \in H_0^u$ and

$$\langle \rho\ddot{u}, v-\dot{u}\rangle + a(\dot{u}, v-\dot{u}) + b(u, v-\dot{u}) + \Phi^u(v,\alpha) - \Phi^u(\dot{u},\alpha) \geq \ell(v-\dot{u}) \quad \forall v \in H_0^u, \tag{32}$$

$$(\dot{\alpha}, \beta-\alpha)_{L^2(\Gamma^F)} + \Psi^u(\beta,\dot{u}) - \Psi^u(\alpha,\dot{u}) \geq 0 \quad \forall \beta \in L^2(\Gamma^F) \tag{33}$$

holds for almost all $t \in (0,T_0)$ together with initial conditions

$$u(0) = u_0, \quad \dot{u}(0) = \dot{u}_0, \quad \alpha(0) = \alpha_0 \tag{34}$$

with given $u_0 \in H_0^{u_0}$ and $\dot{u}_0 \in H_0^{u_0}$ and $\alpha_0 \in L^2(\Gamma^F)$.

It is natural to start the evolution out of an equilibrium configuration, i.e., with an initial displacement u_0 that solves the stationary problem

$$u_0 \in H_0^{u_0}: \qquad b(u_0, v) = \ell(v) \qquad \forall v \in H_0^{u_0}. \tag{35}$$

In our numerical experiments to be reported below, Eq. 35 is solved iteratively by a fixed point iteration over the geometric nonlinearity, i.e., starting with $u_0^0 = 0$, a new iterate $u_0^{\nu+1}$ is computed as the (up to tangential rigid body motions) unique solution of the corresponding linear problem on $H_0^{u_0^\nu}$.

To our knowledge, existence and uniqueness of solutions of Problem 2 is widely open. In case of unilateral frictional contact with a rigid foundation and Dieterich's law Eq. 16, long-time existence of solutions was established by Pipping [31].

3 Semi-discretization in time

Based on the variational approach introduced in the previous section we will now consider the discretization in space and time. To this end we introduce a semi-discretization in time in the present section, while the next section will be devoted to extending this by a spatial discretization. For the temporal discretization we first investigate two time-discrete subproblems for the rate $\dot{u}$ with given state α and vice verse, that are then combined to a coupled time-discrete problem.

Utilizing Rothe's method [20, 39], we perform a time discretization of Problem 2 leading to a sequence of continuous spatial problems to be (approximately) solved in each time step. To this end, the time interval $[0, T_0]$ is partitioned into time steps $0 = t_0 < \cdots < t_N = T_0$ with given step size $\tau_n = t_{n+1} - t_n > 0$, and we write $\tau = \tau_n$ for notational convenience.

3.1 Rate problem with given state

We first consider the rate problem Eq. 29 for given state $\alpha \in L^2(\Gamma^F)$. Following [33], we apply the classical Newmark scheme

$$\begin{aligned} \dot{u}_n &= \dot{u}_{n-1} + \tfrac{\tau}{2}\left(\ddot{u}_{n-1} + \ddot{u}_n\right) \\ u_n &= u_{n-1} + \tau\dot{u}_{n-1} + \left(\tfrac{\tau}{2}\right)^2\left(\ddot{u}_{n-1} + \ddot{u}_n\right) \end{aligned}, \qquad n = 1,\ldots,N, \tag{36}$$

which is well-known to be energy-conserving, consistent with second order, and unconditionally stable [17]. Utilizing Eq. 36, we eliminate

$$\begin{aligned} \ddot{u}_n &= \tfrac{2}{\tau}\left(\dot{u}_n - \dot{u}_{n-1}\right) - \ddot{u}_{n-1}, \\ u_n &= u_{n-1} + \tfrac{\tau}{2}(\dot{u}_n + \dot{u}_{n-1}), \end{aligned} \qquad n = 1,\ldots,N, \tag{37}$$

from Eq. 29 at fixed time $t = t_n$ and freeze the solution dependence in the closed-fault condition and in the friction law at u_{n-1} to obtain the spatial variational inequality

$$\dot{u}_n \in H_0^{u_{n-1}}: \quad a_n(\dot{u}_n, v-\dot{u}_n) + \Phi^{u_{n-1}}(v,\alpha) - \Phi^{u_{n-1}}(\dot{u}_n,\alpha) \geq \ell_n(v-\dot{u}_n), \qquad \forall v \in H_0^{u_{n-1}}, \tag{38}$$

for $n = 1,\ldots,N$. Here, we have set

$$a_n(v,w) = \tfrac{2}{\tau}(\rho v, w) + a(v,w) + \tfrac{\tau}{2}b(v,w) \tag{39}$$

with $(\cdot,\cdot)$ denoting the canonical scalar product in $L^2(\Omega)$ and

$$\ell_n(v) = \ell(v) + (\rho\ddot{u}_{n-1}, v) + \tfrac{2}{\tau}(\rho\dot{u}_{n-1}, v) - \tfrac{\tau}{2}b(\dot{u}_{n-1}, v) - b(u_{n-1}, v).$$

Note that $\ddot{u}_0$ is not given as an initial condition in the continuous Problem 2. Assuming initial acceleration towards equilibrium, $\ddot{u}_0$ is therefore computed from the auxiliar problem

$$\ddot{u}_0 \in H_0: \qquad (\rho\ddot{u}_0, v) + b(u_0, v) = \ell(v) \qquad \forall v \in H_0. \tag{40}$$

Note that the jump terms $[\cdot]^u$, the contact boundary $\Gamma^{F,u}$, and the contact mapping π^u are all taken with respect to the last deformed state $(\mathrm{Id} + u_{n-1})(\Gamma^F)$ of the contact boundary. This eliminates the geometric nonlinearity associated with large (relative) deformations of the contact boundary, and we are left with the variational inequality Eq. 38 on the affine subspace $H_0^{u_{n-1}}$ of H_0 to be solved in each time step.

As $a_n(\cdot,\cdot)$ is symmetric and positive definite and $\Phi(\cdot,\alpha)$ is convex, the variational inequality Eq. 38 can be equivalently written as the minimization problem

$$\dot{u}_n \in H_0^{u_{n-1}}: \qquad \mathcal{J}(\dot{u},\alpha) \leq \mathcal{J}(v,\alpha) \qquad \forall v \in H_0^{u_{n-1}} \tag{41}$$

for the corresponding energy functional

$$\mathcal{J}(\upsilon,\alpha)=\tfrac{1}{2}a_n(\upsilon,\upsilon)+\Phi^{u_{n-1}}(\upsilon,\alpha)-\ell_n(\upsilon).$$

The following lemma [12][Theorem 6.49] will be useful to show existence and uniqueness of a solution.

Lemma 1 *Assume that $g:\Gamma^F\times\mathbb{R}^s\to\mathbb{R}$, $s\in\mathbb{N}$, is a non-negative function, such that $g(x,\cdot)$ is lower semicontinuous for almost all $x\in\Gamma^F$. Then the induced functional*

$$\int_{\Gamma^F} g(x,\cdot)\,dx:\quad L^2(\Gamma^F)\to\mathbb{R}\cup\{+\infty\}$$

is lower semicontinuous.

The convex functional $\Phi^{u_{n-1}}(\cdot,\alpha)$ defined in Eq. 27 for the Dieterich–Ruina model Eq. 22 is proper and lower semicontinuous by Lemma 1. Furthermore, by the assumptions on $\boldsymbol{A}$ and $\boldsymbol{B}$, the bilinear form $(\boldsymbol{A}(x)+\frac{\tau}{2}\boldsymbol{B}(x))(\cdot):(\cdot)$ on the symmetric $d\times d$ matrices is symmetric and uniformly elliptic with respect to $x\in\Omega$. The following existence result therefore follows from Korn's second inequality and [13][Lemma 4.1].

Proposition 1 *Let $f\in L^2(\Omega)$ and $f^N\in L^2(\Gamma^N)$. Assume that u_{n-1}, $n=1,\ldots,N$, avoids self-penetration so that the contact mapping $\pi^{u_{n-1}}$ and thus $H_0^{u_{n-1}}$ are well-defined. Then the spatial rate problem Eq. 38 has a unique solution $\dot u_n\in H_0^{u_{n-1}}$ and any given state $\alpha\in L^2(\Gamma^F)$.*

As a consequence of Proposition 1, the solution operator $R:L^2(\Gamma^F)\to H_0^{u_{n-1}}$,

$$L^2(\Gamma^F)\ni\alpha\mapsto R(\alpha)=\dot u_n\in H_0^{u_{n-1}},\tag{42}$$

of the spatial rate problem Eq. 38 is well-defined, if no self-penetration occurs in preceding time steps. This is a strong assumption, as the contact conditions are taken explicitly. Sufficient conditions for non-penetration as well as possible extensions of the model to infinitesimal penetrations are of interest and a topic of future research.

3.2 State problem with given rate

Discretizing the state problem Eq. 33 with given velocity $\dot u_n\in H_0^{u_{n-1}}$ by the implicit Euler method and freezing the state law at u_{n-1} yields the variational inequality

$$\begin{aligned}&\alpha_n\in L^2(\Gamma^F):\\&(\alpha_n,\beta-\alpha_n)_{L^2(\Gamma^F)}+\tau\Psi^{u_{n-1}}(\beta,\dot u)-\tau\Psi^{u_{n-1}}(\alpha_n,\dot u)\\&\qquad\ge(\alpha_{n-1},\beta-\alpha_n)_{L^2(\Gamma^F)}\quad\forall\beta\in L^2(\Gamma^F)\end{aligned}\tag{43}$$

which can be equivalently expressed as the minimization problem

$$\alpha_n\in L^2(\Gamma^F):\quad\mathcal{E}(\alpha_n,\dot u_n)\le\mathcal{E}(\beta,\dot u_n)\qquad\forall\beta\in L^2(\Gamma^F)\tag{44}$$

for the associated energy

$$\mathcal{E}(\beta,\dot u)=\tfrac{1}{2}(\beta,\beta)_{L^2(\Gamma^F)}+\tau\Psi^{u_{n-1}}(\beta,\dot u)-(\alpha_{n-1},\beta)_{L^2(\Gamma^F)}.$$

Both for Dieterich's law Eq. 20 and Ruina's law Eq. 21, the functional $\Psi(\cdot,\dot u)$ defined in Eq. 30 is convex, proper and, by Lemma 1, lower semicontinuous (see the proof of [33][Proposition 4.4] for details). Hence, existence and uniqueness again follows from [13] [Lemma 4.1].

Proposition 2 *Both for Dieterich's law Eq. 20 and Ruina's law Eq. 21, the spatial state problem Eq. 43 has a unique solution $\alpha_n\in L^2(\Gamma^F)$ for $n=1,\ldots,N$ and any given velocity $\dot u\in H_0^{u_{n-1}}$.*

Proposition 2 gives rise to the solution operator $S:H_0^{u_{n-1}}\to L^2(\Gamma^F)$,

$$H_0^{u_{n-1}}\ni\dot u\mapsto S(\dot u)=\alpha_n\in L^2(\Gamma^F),\tag{45}$$

of the spatial state problem Eq. 43.

3.3 Coupled spatial problem

Combining Eqs. 38 and 43, the time discretization of Problem 2 now reads as follows.

Problem 3 (Semi-discretization in time) Find $\dot u_n\in H_0^{u_{n-1}}$ and $\alpha_n\in L^2(\Gamma^F)$ satisfying

$$\begin{aligned}&a_n(\dot u_n,\upsilon-\dot u_n)+\Phi^{u_{n-1}}(\upsilon,\alpha_n)-\Phi^{u_{n-1}}(\dot u_n,\alpha_n)\\&\quad\ge\ell_n(\upsilon-\dot u_n),\qquad\qquad\forall\upsilon\in H_0^{u_{n-1}}\\&(\alpha_n,\beta-\alpha_n)_{L^2(\Gamma^F)}+\tau\Psi^{u_{n-1}}(\beta,\dot u_n)-\tau\Psi^{u_{n-1}}(\alpha_n,\dot u_n)\\&\quad\ge(\alpha_{n-1},\beta-\alpha_n)_{L^2(\Gamma^F)}\qquad\forall\beta\in L^2(\Gamma^F)\end{aligned}$$

for $n=1,\ldots,N$ with $\ddot u_n$ computed from Eq. 37 and the auxiliary problem Eq. 40, and given initial conditions $u_0,\dot u_0\in H_0^{u_0}$, $\alpha_0\in L^2(\Gamma^F)$.

Recall, that $H_0^{u_{n-1}}$ is well-defined only if u_{n-1} avoids self-penetration, because the contact map $\pi^{u_{n-1}}$ is not available otherwise. This drawback could be overcome by introducing an approximate contact map $\tilde\pi$ as in the spatial discretization below.

For an unilateral version of Problem 3, i.e., a subduction zone with rigid foundation and Dieterich's law, such difficulties do not occur and existence and uniqueness have been shown in [30][Proposition 3.6.] based on Banach's fixed point theorem. In case of Ruina's law, existence (but possibly no uniqueness) was established utilizing Schauders fixed point theorem (see [30][Corollary 3.8.] or [33][Theorem 5.14]).

4 Discretization in time and space

The semi-discretization in time given by Problem 3 forms the basis of a full discretization in space and time to be introduced in the present section. Individual layers are discretized using a finite element ansatz and the non-penetration between layers is enforced weakly using a mortar approach with dual mortar test functions. Again we will first consider two subproblems: A rate problem with given state and a state problem with given rate. For the coupled, fully discrete problem we then propose a fixed point iteration where each step can be decomposed into these two subproblems.

For each $i = 1, \dots, I$ we assume that the subdomain Ω_i is polygonal and denote by $\mathcal{T}_i$ a triangulation, i.e., a shape-regular, simplicial partition, of Ω_i with vertices $\mathcal{N}_i^*$. We introduce the associated vector-valued, linear finite element space

$$\mathcal{S}_i = \left\{ v \in C(\Omega_i)^d \mid v \text{ is linear on all } T \in \mathcal{T}_i \text{ and } v|_{\Gamma_i^D} = 0 \right\}.$$

Assuming that the Dirichlet boundary Γ_i^D is resolved by $\mathcal{T}_i$, we define the set of nodes $\mathcal{N}_i = \mathcal{N}_i^* \setminus \overline{\Gamma_i^D}$. The resulting partition $\mathcal{T} = \bigcup_{i=1}^I \mathcal{T}_i$ of Ω leads to the associated product space

$$\mathcal{S} = \mathcal{S}_1 \times \cdots \times \mathcal{S}_I = \operatorname{span}\{\lambda_p e_j \mid p \in \mathcal{N}, \; j = 1, \dots, d\} \subset H_0$$

with the nodes $\mathcal{N} = \bigcup_{i=1}^I \mathcal{N}_i$, the nodal basis functions $\lambda_p \in \mathcal{S}_i$, $p \in \mathcal{N}_i$, and the unit vectors $e_j \in \mathbb{R}^d$, $j = 1, \dots, d$. We emphasize that the triangulations $\mathcal{T}_i$ and $\mathcal{T}_{i+1}$ do not need to match at the common interface $\Gamma_{i,i+1}^F$, $i = 1, \dots I-1$, in the sense that the sets $\mathcal{N}_i \cap \Gamma_{i,i+1}^F$ and $\mathcal{N}_{i+1} \cap \Gamma_{i,i+1}^F$ in general do not coincide. For ease of notation, we even assume $\mathcal{N}_i \cap \mathcal{N}_j = \emptyset$ for $i \neq j$ so that we do not need to distinguish shared nodes and unshared nodes in the following presentation.

4.1 Mortar discretization of rate problem with given state

We consider the spatial rate problem Eq. 38 with given state $\alpha \in L^2(\Gamma^F)$.

In order to incorporate non-penetration and tangential friction along the fault system Γ^F, we first introduce its triangulation

$$\mathcal{T}^F = \bigcup_{i=1}^{I-1} \mathcal{T}_i^F, \qquad \mathcal{T}_i^F = \{F = T \cap \Gamma_{i,i+1}^F \mid T \in \mathcal{T}_i\},$$

with the nodes $\mathcal{N}^F = \bigcup_{i=1}^{I-1} \mathcal{N}_i^F$, $\mathcal{N}_i^F = \mathcal{N}_i \cap \Gamma_{i,i+1}^F$, together with the corresponding trace space

$$\mathcal{S}^F = (v_1, \dots, v_{I-1}) \subset L^2(\Gamma^F)^d, \qquad v_i \in \mathcal{S}_i^F = \mathcal{S}_i|_{\Gamma_{i,i+1}^F},$$

spanned by the nodal basis $\lambda_p e_j|_{\Gamma^F}$, $p \in \mathcal{N}^F$, $j = 1, \dots, d$. Note that the triangulation $\mathcal{T}_i^F$ and the associated finite element trace space $\mathcal{S}_i^F$ on $\Gamma_{i,i+1}^F$ are inherited from Ω_i (the bottom non-mortar side), and do not coincide with corresponding traces from Ω_{i+1} (the top mortar side).

Mimicking the continuous case, the discretization of non-penetration condition and friction law is based on an approximation $\tilde{\pi} : \tilde{\Gamma}_B^F \to \tilde{\Gamma}_T^F$ of the contact mapping of $\pi^{u_{n-1}}$ from the preceding time step with corresponding approximations $\tilde{\Gamma}_B^F \subset \Gamma^F$, and $\tilde{\Gamma}_T^F \subset \Gamma^F$ of $\Gamma_B^{F,u_{n-1}}$, and $\Gamma_T^{F,u_{n-1}}$, respectively. The approximations $\tilde{\pi}$ and $\tilde{\Gamma}_B^F$ come into play, because the top and bottom interfaces of the deformed subdomains $(\mathrm{Id} + u_{n-1,i})(\Omega_i)$ may not match due to discretization errors that arise from enforcing non-penetration for u_{n-1}. In the following, we assume that the non-mortar contact boundary $\tilde{\Gamma}_B^F$ is resolved by a subset of the fault triangulation $\mathcal{T}^F$. We refer to [5, 42] and the references cited therein for algorithms to compute such approximations of non-matching discrete intersections.

In analogy to Eq. 1 the jump of $v \in \mathcal{S}$ across the discrete deformed contact boundary is then defined by

$$\widetilde{[v]} = v_B - v_T \circ \tilde{\pi} \qquad \text{on } \tilde{\Gamma}_B^F.$$

In the spirit of [49], the non-penetration condition appearing in Eq. 23 and the (tangential) jumps appearing in the functionals $\Phi^{u_{n-1}}$ and $\Psi^{u_{n-1}}$ of the Dieterich–Ruina model will be incorporated in a weak sense with respect to a discrete test space spanned by dual mortar basis functions as introduced by Wohlmuth [47].

To this end, we first introduce the set of non-mortar contact nodes

$$\tilde{\mathcal{N}}^F = \mathcal{N}^F \cap \overline{\tilde{\Gamma}_B^F}$$

as well as the deformed contact set

$$\tilde{\mathcal{C}} = (\mathrm{Id} + u_{n-1,B})(\tilde{\Gamma}_B^F),$$

and we work with the pullback of the $L^2(\tilde{\mathcal{C}})$ inner product to $\tilde{\Gamma}^F_B$

$$\langle v, w\rangle_{\tilde{\mathcal{C}}} = (v \circ (\mathrm{Id} + u_{n-1,B})^{-1}, w \circ (\mathrm{Id} + u_{n-1,B})^{-1})_{L^2(\tilde{\mathcal{C}})}.$$

Then the dual mortar basis functions $\varphi_q, q \in \widetilde{\mathcal{N}}^F$, are defined to be piecewise linear on $\mathcal{T}^F$, have the same support as $\lambda_q|_{\Gamma^F}$, and satisfy the bi-orthogonality property

$$\langle \lambda_p|_{\Gamma^F}, \varphi_q\rangle_{\tilde{\mathcal{C}}} = \delta_{p,q} \qquad \forall p, q \in \widetilde{\mathcal{N}}^F \qquad \text{(Kronecker-}\delta\text{)}.$$

Note that dual mortar functions are typically discontinuous and therefore not contained in $\mathcal{S}^F$. We refer to [47, 48] for details about the construction.

We now define the linear projection $\Pi : \mathcal{S} \to \mathcal{S}$, componentwise according to

$$(\Pi v)_j = \Pi v_j = v_j - \sum_{p\in\widetilde{\mathcal{N}}^F} \langle \widetilde{[v_j]}, \varphi_p\rangle_{\tilde{\mathcal{C}}}\lambda_p, \qquad j = 1, \ldots d.$$

Observe that here and in the following we denote by Π the projection of both scalar and $\mathbb{R}^d$-valued functions. The projection Π gives rise to the direct splitting

$$\mathcal{S} = \mathcal{V} \oplus \mathcal{W}$$

of $\mathcal{S}$ into the image $\mathcal{V} = \mathrm{im}\Pi$ and the kernel $\mathcal{W} = \ker\Pi$ of Π. Utilizing the fact that $\widetilde{[\lambda_p]} = \lambda_p$ for $p \in \widetilde{\mathcal{N}}^F$, we find that these spaces can be written as

$$\begin{aligned}\mathcal{V} &= \left\{ v \in \mathcal{S} \;\middle|\; \langle\widetilde{[v]}, \varphi_p\rangle_{\tilde{\mathcal{C}}} = 0 \;\forall p \in \widetilde{\mathcal{N}}^F \text{ and } j = 1, \ldots, d \right\}\\ &= \operatorname{span}\left\{ \mu_p e_j \;\middle|\; \mu_p = \Pi\lambda_p,\;\; p \in \mathcal{N}\setminus\widetilde{\mathcal{N}}^F \text{ and } j = 1, \ldots, d \right\}\end{aligned}$$

and

$$\begin{aligned}\mathcal{W} &= \left\{ v \in \mathcal{S} \;\middle|\; v(p) = 0 \;\forall p \in \mathcal{N}\setminus\widetilde{\mathcal{N}}^F \right\}\\ &= \operatorname{span}\left\{ \lambda_p e_j \;\middle|\; p \in \widetilde{\mathcal{N}}^F \text{ and } j = 1, \ldots, d \right\}.\end{aligned}$$

Thus, $\mathcal{V}$ consists of all functions in $\mathcal{S}$ which are weakly continuous across the deformed contact boundary with respect to the pullback L^2 scalar product $\langle\cdot,\cdot\rangle_{\tilde{\mathcal{C}}}$ and the associated dual mortar space (notice that point-wise continuity does not hold in general).

Correspondingly, the basis functions $\mu_p = \Pi\lambda_p$ spanning $\mathcal{V}$ are the usual hat functions λ_p on the mortar side, which are extended in a weakly continuous way to the non-mortar side, while the basis functions $\lambda_p e_j$ of $\mathcal{W}$ involve the usual hat functions λ_p, $p \in \widetilde{\mathcal{N}}^F$ on the non-mortar side which drop down to zero across $\tilde{\Gamma}^F_B$.

Both normal and tangential jumps of $v \in \mathcal{V}$ are weakly zero. As a consequence, both (weak) normal and tangential jumps can be represented in terms of the incremental space $\mathcal{W}$. To this end, we define a nodal approximation $n_{\mathcal{S}}$ of the normal to the deformed contact set $\tilde{\mathcal{C}}$ by

$$n_{\mathcal{S}} = \sum_{p\in\widetilde{\mathcal{N}}^F} n_p\lambda_p|_{\tilde{\Gamma}^F_B}, \qquad n_p = \frac{\sum_{F\in\mathcal{T}^F_p} n_F}{|\sum_{F\in\mathcal{T}^F_p} n_F|}, \tag{46}$$

where $\mathcal{T}^F_p$ denotes the set of simplices $F \in \mathcal{T}^F_i$ with common vertex $p \in \widetilde{\mathcal{N}}^F$, and n_F is an approximate normal to the deformed face $(\mathrm{Id} + u_{n-1})_B(F)$, e.g. the average of the normal on $(\mathrm{Id} + u_{n-1})_B(F)$. We also introduce the approximate tangent space $T_p\tilde{\mathcal{C}} = (\operatorname{span}\{n_p\})^{\perp} \subset \mathbb{R}^d$ to the deformed contact set $\tilde{\mathcal{C}}$ associated with the nodal approximate normal n_p in $p \in \widetilde{\mathcal{N}}^F$. Similar to the continuous case, the discrete normal field $n_{\mathcal{S}}$ to $\tilde{\mathcal{C}}$ is parametrized over $\tilde{\Gamma}^F_B$.

Next, we further split $\mathcal{W}$ into its normal and tangential part

$$\mathcal{W} = \mathcal{W}_n \oplus \mathcal{W}_t,$$

with

$$\begin{aligned}\mathcal{W}_n &= \left\{ \lambda_p x \;\middle|\; p \in \widetilde{\mathcal{N}}^F, x \in \operatorname{span}\{n_p\} \right\},\\ \mathcal{W}_t &= \left\{ \lambda_p x \;\middle|\; p \in \widetilde{\mathcal{N}}^F, x \in T_p\tilde{\mathcal{C}} \right\}.\end{aligned}$$

Excluding normal jumps, we now define a (non-conforming) finite element counterpart of the solution space $H_0^{u_{n-1}}$ according to

$$\mathcal{S}_0^{u_{n-1}} = \mathcal{V} \oplus \mathcal{W}_t. \tag{47}$$

Such a mortar approach to non-penetration has been suggested and first analyzed in [47].

The splitting suggests the unique decomposition

$$v = v_{\mathcal{V}} + v_{\mathcal{W}}, \qquad v \in \mathcal{S}_0^{u_{n-1}} \tag{48}$$

where

$$v_{\mathcal{V}} = \Pi v = \sum_{\mathcal{N}\setminus\widetilde{\mathcal{N}}^F} v(p)\mu_p \in \mathcal{V}$$

and

$$v_{\mathcal{W}} = (\mathrm{Id} - \Pi)v = \sum_{p\in\widetilde{\mathcal{N}}^F} [v]_p\lambda_p \in \mathcal{W}_t,$$

denoting the weak nodal jump of v at $p \in \widetilde{\mathcal{N}}^F$ by

$$[v]_p = (v - \Pi(v))(p) = (\langle\widetilde{[v_j]}, \varphi_p\rangle_{\tilde{\mathcal{C}}})_{j=1}^d \in \mathbb{R}^d.$$

The nodal vectors $[\upsilon]_p$ clearly satisfy $[\upsilon]_p \cdot n_p = 0$ for all $p \in \tilde{\mathcal{N}}^F$. Hence, $\upsilon_{\mathcal{W}}$ can be regarded as a nodal approximation of the tangential jump of υ along $\tilde{\mathcal{C}}$ pulled back to $\tilde{\Gamma}_B^F$. Inserting this approximation into Eq. 27 and replacing the integrand $\phi([\upsilon]^u, \alpha)$ by its nodal interpolation in $\mathcal{S}^F$, we obtain the approximate functional $\Phi_{\mathcal{S}} : \mathcal{S}_0^{u_{n-1}} \to \mathbb{R}$,

$$\Phi_{\mathcal{S}}(\upsilon, \alpha) = \sum_{p \in \tilde{\mathcal{N}}^F} \phi_p([\upsilon]_p),$$

$$\phi_p([\upsilon]_p) = \phi([\upsilon]_p, \alpha(p)) \int_{\tilde{\Gamma}_B^F} \lambda_p \, ds. \tag{49}$$

At this point, α is required to be continuous in a neighborhood of each node $p \in \tilde{\mathcal{N}}^F$ to guarantee that nodal interpolation makes sense.

The mortar discretization of the rate problem Eq. 38 with given, sufficiently regular state $\alpha \in L^2(\Gamma^F)$ now reads as follows

$$\dot{u}_{n,\mathcal{S}} \in \mathcal{S}_0^{u_{n-1}} : \quad a_n(\dot{u}_{n,\mathcal{S}}, \upsilon - \dot{u}_{n,\mathcal{S}}) + \Phi_{\mathcal{S}}(\upsilon, \alpha) \\ -\Phi_{\mathcal{S}}(\dot{u}_{n,\mathcal{S}}, \alpha) \geq \ell_{n,\mathcal{S}}(\upsilon - \dot{u}_{n,\mathcal{S}}), \qquad \forall \upsilon \in \mathcal{S}_0^{u_{n-1}}, \tag{50}$$

for $n = 1, \dots, N$. Here, the bilinear form $a_n(\cdot, \cdot)$ is taken from Eq. 39 and we have set

$$\ell_{n,\mathcal{S}}(\upsilon) = \ell(\upsilon) + (\rho \ddot{u}_{n-1,\mathcal{S}}, \upsilon) + \tfrac{2}{\tau}(\rho \dot{u}_{n-1,\mathcal{S}}, \upsilon) \\ -\tfrac{\tau}{2} b(\dot{u}_{n-1,\mathcal{S}}, \upsilon) - b(u_{n-1,\mathcal{S}}, \upsilon)$$

with $\ddot{u}_{n-1,\mathcal{S}}$, $\dot{u}_{n-1,\mathcal{S}}$, $u_{n-1,\mathcal{S}}$ taken from preceding time steps, by discrete analogues of Eq. 37, by suitable finite element approximations $\dot{u}_{0,\mathcal{S}}, u_{0,\mathcal{S}} \in \mathcal{S}$ of the initial conditions $\dot{u}_0, u_0 \in H_0^{u_0}$, or a finite element approximation $\ddot{u}_{0,\mathcal{S}} \in \mathcal{S}$ of the auxiliary problem Eq. 40. Existence and uniqueness of discrete spatial solutions $\dot{u}_{n,\mathcal{S}} \in \mathcal{S}_0^{u_{n-1}}$, $n = 1, \dots, N$, follows under the same conditions and by the same arguments as in Proposition 1.

This mortar approach to (frictional) non-penetration directly extends elastic frictional contact problems, i.e., to fault opening. We refer to [22, 24] for further information and to [48] for a detailed survey.

4.2 Piecewise constant discretization of state problem with given rate

We consider the state problem Eq. 43 with a given deformation rate. Let $\mathcal{C}^F = \{C_p \subset \Gamma^F \mid p \in \mathcal{N}^F\}$ be a dual partition of the triangulation $\mathcal{T}^F$ of Γ^F. We introduce the subspace $\mathcal{B}^F \subset L^2(\Gamma^F)$ of functions that are constant on each cell $C_p \in \mathcal{C}^F$, $p \in \mathcal{N}^F$, and the resulting piecewise constant discretization

$$\alpha_{n,\mathcal{B}} \in \mathcal{B}^F : \\ \left(\alpha_{n,\mathcal{B}}, \beta - \alpha_{n,\mathcal{B}}\right)_{L^2(\Gamma^F)} + \tau \Psi_{\mathcal{B}}(\beta, \dot{u}) - \tau \Psi_{\mathcal{B}}(\alpha_{n,\mathcal{B}}, \dot{u}) \\ \geq \left(\alpha_{n-1,\mathcal{B}}, \beta - \alpha_{n,\mathcal{B}}\right)_{L^2(\Gamma^F)} \qquad \forall \beta \in \mathcal{B}^F \tag{51}$$

of the state problem Eq. 43 with given $\dot{u} \in \mathcal{S}_0^{u_{n-1}}$. Here, the nodal approximation $\Psi_{\mathcal{B}} : \mathcal{B}^F \to \mathbb{R}$,

$$\Psi_{\mathcal{B}}(\beta, \dot{u}) = \sum_{p \in \tilde{\mathcal{N}}^F} \psi(\beta(p), |[\dot{u}]_p|) \left|C_p\right|, \qquad \beta \in \mathcal{B}^F, \tag{52}$$

of the functional $\Psi(\cdot, \dot{u})$ is obtained in the same way as the nodal approximation $\Phi_{\mathcal{S}}(\cdot, \alpha)$ of $\Phi(\cdot, \alpha)$ in Eq. 49.

Existence and uniqueness of discrete spatial solutions $\alpha_{n,\mathcal{B}} \in \mathcal{B}^F$, $n = 1, \dots, N$, follows in the same way as in Proposition 2.

4.3 Fully discretized coupled spatial problem

Combining Eqs. 50 and 51, the discretization of the coupled Problem 2 in time and space now reads as follows.

Problem 4 (Discretization in time and space) Find $\dot{u}_{n,\mathcal{S}} \in \mathcal{S}_0^{u_{n-1}}$ and $\alpha_{n,\mathcal{B}} \in \mathcal{B}^F$ satisfying

$$a_n(\dot{u}_{n,\mathcal{S}}, \upsilon - \dot{u}_{n,\mathcal{S}}) + \Phi_{\mathcal{S}}(\upsilon, \alpha_{n,\mathcal{B}}) - \Phi_{\mathcal{S}}(\dot{u}_{n,\mathcal{S}}, \alpha_{n,\mathcal{B}}) \\ \geq \ell_{n,\mathcal{S}}(\upsilon - \dot{u}_{n,\mathcal{S}}) \qquad \forall \upsilon \in \mathcal{S}_0^{u_{n-1}} \\ \left(\alpha_{n,\mathcal{B}}, \beta - \alpha_{n,\mathcal{B}}\right)_{L^2(\Gamma^F)} + \tau \Psi_{\mathcal{B}}(\beta, \dot{u}_{n,\mathcal{S}}) - \tau \Psi_{\mathcal{B}}(\alpha_{n,\mathcal{B}}, \dot{u}_{n,\mathcal{S}}) \\ \geq \left(\alpha_{n-1,\mathcal{B}}, \beta - \alpha_{n,\mathcal{B}}\right)_{L^2(\Gamma^F)} \quad \forall \beta \in \mathcal{B}^F$$

for $n = 1, \dots, N$ with given initial conditions $u_{0,\mathcal{S}}, \dot{u}_{0,\mathcal{S}} \in \mathcal{S}_0^{u_{n-1}}$, $\alpha_{0,\mathcal{B}} \in \mathcal{B}^F$.

Iterative solution of Problem 4 can be obtained from the fixed point iteration

$$\dot{u}_{n,\mathcal{S}}^{\nu+1} = R_{\mathcal{S}}\left(\omega \alpha_{n,\mathcal{B}}^{\nu+1} + (1-\omega)\alpha_{n,\mathcal{B}}^{\nu}\right), \\ \alpha_{n,\mathcal{B}}^{\nu+1} = S_{\mathcal{B}}\left(\dot{u}_{n,\mathcal{S}}^{\nu}\right), \quad \nu = 0, 1, \dots, \tag{53}$$

with initial iterate $(\dot{u}_{n,\mathcal{S}}^0, \alpha_{n,\mathcal{B}}^0) = (\dot{u}_{n-1,\mathcal{S}}, \alpha_{n-1,\mathcal{B}})$ and suitable relaxation parameter $\omega \in (0, 1]$. Here, $S_{\mathcal{B}} : \mathcal{S}_0^{u_{n-1}} \to \mathcal{B}^F$ and $R_{\mathcal{S}} : \mathcal{B}^F \to \mathcal{S}_0^{u_{n-1}}$ denote the solution operators of the state problem with given rate Eq. 51 and the rate problem with given state Eq. 50, respectively. Note that state functions $\alpha \in \mathcal{B}^F$ are continuous in a neighborhood of each node $p \in \mathcal{N}^F$ and thus satisfy the regularity assumptions made for nodal interpolation Eq. 49.

Extension of the convergence proof given in [30, 33] for an unilateral version of Problem 4 to the actual discretized multi-body problem is a subject of future research.

5 Algebraic solution

We will now discuss the algebraic solution of the coupled fully discrete Problem 4. After decoupling the problem using a fixed point iteration we are left with a sequence of discrete rate and state subproblems. While the state problems can be solved explicitly, we will adapt the Truncated Nonsmooth Newton Multigrid (TNNMG) methods [14–16] for the non-smooth nonlinear rate subproblems.

5.1 Fixed point iteration and state problem with given rate

The iterative solution of the coupled Problem 4 is performed by the fixed point iteration Eq. 53. The state problem with given rate Eq. 51 arising in each iteration step fully decouples into scalar algebraic problems for $\alpha_{n,\mathcal{B}}(p)$ and $p \in \mathcal{N}^F$ that can be solved explicitly or, e.g., by bisection.

The rate problem with given state Eq. 50, however, is a discretized frictional contact problem, and its iterative solution is more involved.

5.2 Truncated Nonsmooth Newton multigrid for the rate problem with given state

We now concentrate on the robust and efficient algebraic solution of the mortar-discretized rate problem Eq. 50 with given state $\alpha \in \mathcal{B}^F$. First, recall that the splitting Eq. 48 provides the basis representation

$$\upsilon = \sum_{p \in \mathcal{N} \setminus \widetilde{\mathcal{N}}^F} \upsilon_p \mu_p + \sum_{p \in \widetilde{\mathcal{N}}^F} \upsilon_p \lambda_p \tag{54}$$

of all $\upsilon \in \mathcal{S}_0^{u_{n-1}}$ with coefficients $\upsilon_p = \upsilon(p)$, $p \in \mathcal{N} \setminus \widetilde{\mathcal{N}}^F$ and $\upsilon_p = [\upsilon]_p$, $p \in \widetilde{\mathcal{N}}^F$. We identify each $\upsilon \in \mathcal{S}_0^{u_{n-1}}$ with its coefficient vector $(\upsilon_p)_{p \in \mathcal{N}}$. Then the discrete nonlinear functional

$$\Phi_{\mathcal{S}}(\upsilon, \alpha) = \sum_{p \in \widetilde{\mathcal{N}}^F} \phi_p(\upsilon_p)$$

introduced in Eq. 49 has a separable structure in the sense that the coefficients $\upsilon_p \in \mathbb{R}^d$ are decoupled with respect to the nonlinearity ϕ_p.

The variational inequality Eq. 50 can be equivalently rewritten as the minimization problem

$$\dot{u}_{n,\mathcal{S}} \in \mathcal{S}_0^{u_{n-1}} : \qquad \mathcal{J}_{\mathcal{S}}(\dot{u}_{n,\mathcal{S}}) \leq \mathcal{J}_{\mathcal{S}}(\upsilon) \qquad \forall \upsilon \in \mathcal{S}_0^{u_{n-1}} \tag{55}$$

denoting

$$\mathcal{J}_{\mathcal{S}}(\upsilon) = \tfrac{1}{2} a_n(\upsilon, \upsilon) - \ell_{n,\mathcal{S}}(\upsilon) + \sum_{p \in \widetilde{\mathcal{N}}^F} \phi_p(\upsilon_p).$$

This formulation allows to construct and analyze globally convergent nonlinear Gauß–Seidel relaxation methods [13]. Based on the splitting

$$\mathcal{S}_0^{u_{n-1}} = \sum_{p \in \mathcal{N}} \mathcal{V}_p, \qquad \mathcal{V}_p = \begin{cases} \{\mu_p x \mid x \in \mathbb{R}^d\} & \text{for } p \in \mathcal{N} \setminus \widetilde{\mathcal{N}}^F, \\ \{\lambda_p x \mid x \in T_p \tilde{\mathcal{C}}\} & \text{for } p \in \widetilde{\mathcal{N}}^F \end{cases}$$

and some enumeration $\mathcal{N} = \{p_1, \ldots, p_M\}$, a new iterate is computed by successive subspace minimization: Given an iterate u set $w_0 = u$ and compute w_i, $i = 1, \ldots, M$ by solving

$$\begin{aligned} &w_i \in w_{i-1} + \mathcal{V}_{p_i} : \ \ \mathcal{J}_{\mathcal{S}}(w_i) \leq \mathcal{J}_{\mathcal{S}}(w) \ \ \forall w \in w_{i-1} + \mathcal{V}_{p_i}, \\ &\quad i = 1, \ldots, M, \end{aligned} \tag{56}$$

to obtain the new iterate $\bar{u} = w_M$. However, such iterative schemes are well-known to suffer from rapidly deteriorating convergence rates for decreasing mesh size.

The basic idea of *Truncated Nonsmooth Newton Multigrid* (TNNMG) methods [14–16] is to complement nonlinear Gauß–Seidel smoothing Eq. 56 by additional line search into the Newton-type search direction δu, as obtained from the linear system

$$\mathcal{J}_{\mathcal{S}}''(\bar{u})|_{W(\bar{u}) \times W(\bar{u})} \delta u = -\mathcal{J}_{\mathcal{S}}'(\bar{u})|_{W(\bar{u})} \tag{57}$$

on a suitable subspace $W(\bar{u}) \subset \mathcal{S}_0^{u_{n-1}}$. Accounting for non-smoothness of ϕ_p, $p \in \widetilde{\mathcal{N}}^F$, we select the reduced subspace

$$\begin{aligned} W(\bar{u}) = \mathcal{V} + \operatorname{span}\{\lambda_p x \mid \\ &x \in T_p \tilde{\mathcal{C}}, |[\bar{u}]_p| \neq V_m(\alpha(p)), p \in \widetilde{\mathcal{N}}^F\}. \end{aligned}$$

By freezing $\bar{u}(p)$ at those p where $\phi_p(\bar{u}_p)$ is not smooth enough, the restriction $\mathcal{J}_{\mathcal{S}}|_{W(\bar{u}) \times W(\bar{u})}$ to $W(\bar{u})$ is twice differentiable. Note that global convergence of nonlinear Gauß–Seidel smoothing Eq. 56 is preserved by any correction $\rho \delta u$ such that $\rho \in [0, \infty)$ is providing non-increasing energy

$$\mathcal{J}_{\mathcal{S}}(\bar{u} + \rho \delta u) \leq \mathcal{J}_{\mathcal{S}}(\bar{u}). \tag{58}$$

In TNNMG methods, all three substeps, i.e., nonlinear Gauß–Seidel relaxation Eq. 56, evaluation of the Newton-type search direction Eq. 57, and monotone line search Eq. 58, are typically performed inexactly. A TNNMG iteration step applied to a given iterate $u^\nu \in \mathcal{S}_0^{u_{n-1}}$ thus reads as follows

$$\begin{aligned}\bar{u}_\nu &= P(u^\nu),\\ \delta u^\nu &= MG(\mathcal{J}''_{\mathcal{S}}(\bar{u}_\nu)|_{W(\bar{u}_\nu)\times W(\bar{u}_\nu)}, \mathcal{J}'_{\mathcal{S}}(\bar{u}_\nu)|_{W(\bar{u}_\nu)}),\\ u^{\nu+1} &= \bar{u}_\nu + \rho(\bar{u}_\nu, \delta u^\nu)\delta u^\nu, \end{aligned} \tag{59}$$

with corresponding inexact solution operators P, MG, and ρ.

More precisely, inexact Gauß–Seidel relaxation P is obtained as follows. For each convex $(d-1)$-dimensional nonsmooth minimization problem Eq. 56 on the local tangent space $\mathcal{V}_{p_i}$ associated with the node $p_i \in \widetilde{\mathcal{N}}^F$, the quadratic part (i.e., the i-th diagonal block of the stiffness matrix corresponding to the bilinear form $a_n(\cdot,\cdot)$ and the basis representation Eq. 54) is replaced by a scalar upper bound, e.g. its maximal eigenvalue. Then the resulting problem is rotationally symmetric in $\mathcal{V}_{p_i}$ and thus reduces to a scalar problem that can be solved by bisection or even by an explicit formula (cf. [16][Example 5.2]). The same local preconditioning approach is used for the linear d-dimensional problems in $\mathcal{V}_{p_i}$ for $p_i \in \mathcal{N}\setminus\widetilde{\mathcal{N}}^F$. We emphasize that global convergence of nonlinear Gauß–Seidel relaxation Eq. 56 is preserved in this way [16].

Since $\mathcal{J}_{\mathcal{S}}$ is strongly convex, the coefficient matrix $\mathcal{J}''_{\mathcal{S}}(\bar{u}_\nu)|_{W(\bar{u}_\nu)\times W(\bar{u}_\nu)}$ of the linear problem Eq. 57 is symmetric and positive definite on the subspace $W(\bar{u}_\nu)$. Hence, its inexact solution MG can be simply performed by one or more steps of a standard linear multigrid method with minor modifications to deal with the special basis used in Eq. 54 and the restriction to $W(\bar{u}_\nu)$. For details on the choice of suitable coarse grid spaces or, equivalently, suitable restriction and prolongation operators we refer, e.g., to [15, 41].

Inexact line search providing a damping factor $\rho_\nu \in [0,\infty)$ that guarantees monotonically decreasing energy Eq. 58 is finally performed by bisection.

The following convergence result is obtained as a special case of the abstract result [16] [Corollary 4.5] by making use of [16] [Theorem 5.6 and Lemma 5.8] to incorporate the inexact pre-smoothing P explained above.

Proposition 3 *For any initial iterate $u^0 \in \mathcal{S}_0^{u_{n-1}}$ the sequence $u^\nu \in \mathcal{S}_0^{u_{n-1}}$, $\nu = 1,\dots,$ generated by the TNNMG method Eq. 59 converges to the unique solution of the mortar-discretized rate problem Eq. 50 with given state $\alpha \in \mathcal{B}^F$.*

The same convergence result applies, if more than one nonlinear pre-smoothing step or additional nonlinear post-smoothing is utilized. Note that TNNMG methods allow for straightforward extensions to fault opening by incorporating non-penetration into the nonlinear Gauß–Seidel smoother and enforcing feasibility of coarse corrections δu^ν by an additional projection step.

6 Numerical experiments

The characteristic behaviour of the introduced variational multi-layer model and the performance of the proposed numerical methods will now be investigated using two numerical experiments. After introducing the general setup, we first consider a spring slider with two bodies and then a layered fault system with five bodies. For both experiments we discuss the behaviour of the model in terms of the observed slip events and the numerical performance of the adaptive time stepping scheme, the fixed point iteration, and the nonlinear multigrid method.

6.1 General setup

While both our mathematical model and our numerical solution methods have been derived for $d = 2, 3$ space dimensions, we only concentrate on $d = 2$ for reasons of computational complexity. Indeed, in spite of satisfying solver performance (see, e.g., Fig. 6 below), substantial numerical experiments in $d = 3$ space dimensions would require parallelization and other supercomputing techniques to achieve reasonable computing times, cf., e.g., [18, 26, 28].

6.1.1 Problem description

In our two numerical experiments, we consider a rectangular deformable body in $d = 2$ space dimensions that is decomposed into $I = 2$ (spring slider) or $I = 5$ (layered fault system) rectangular bodies by 1 or 4 planar faults, cf. Fig. 2.

In the spring slider experiment, the 2 bodies are both of the size $5m \times 1m$. They are associated with the reference domains $\Omega_1 = (-2.5, 2.5)\times(-1,0)$, $\Omega_2 = (-2.5, 2.5)\times(0,1)$ with the interface

$$\Gamma^F = (-2.5, 2.5)\times\{0\}.$$

This setup corresponds to the one presented in [33], but features a deformable instead of a rigid foundation.

The bodies of the layered fault system have the size 5m × 1m, 5m × 0.3m, 5m × 0.09m, 5m × 0.3m, and 5m × 1m. They are associated with the reference domains

$$\Omega_1 = (-2.5, 2.5)\times(-1.345, -0.345),\quad \Omega_2 = (-2.5, 2.5)\times(-0.345, -0.045),$$
$$\Omega_3 = (-2.5, 2.5)\times(-0.045, 0.045),\quad \Omega_4 = (-2.5, 2.5)\times(0.045, 0.345),$$
$$\Omega_5 = (-2.5, 2.5)\times(0.345, 1.345)$$

with the interface Γ^F,

$$\begin{aligned}\Gamma^F &= (-2.5, 2.5)\times\{-0.345\}\cup(-2.5, 2.5)\times\{-0.045\}\\ &\quad\cup(-2.5, 2.5)\times\{0.045\}\cup(-2.5, 2.5)\times\{0.345\}.\end{aligned}$$

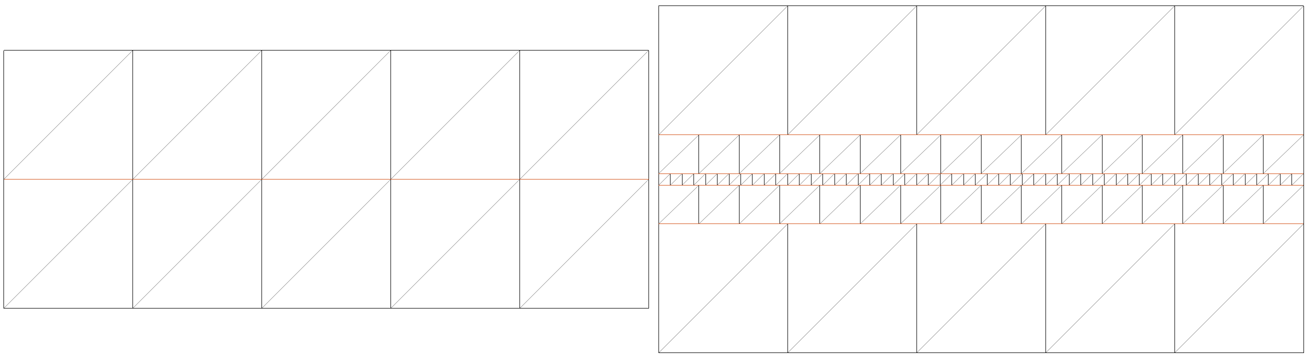

Fig. 2 Initial triangulations $\mathcal{T}_i^{(0)}, i = 1, \dots, I$, for the spring slider with $I = 2$ bodies (left) and a layered fault system with $I = 5$ bodies (right)

The bodies consist of St. Venant Kirchhoff material and are subject to gravity, i.e., the body force is constant and given by $f = -\rho g \cdot e_2$ with g denoting the gravitational constant. We impose homogeneous Neumann boundary conditions $f^N = 0$ at the vertical boundary Γ^N of the associated reference configurations $\Omega_i, i = 1, \dots, I$. The system is fixed by homogeneous Dirichlet conditions $u(\cdot, t) = \dot{u}(\cdot, t) = 0$, $0 \leq t \leq T_0$ at the foundation Γ_1^D. At the upper Dirichlet boundary $\Gamma_I^D, I = 2,\ 5$, the condition $\dot{u}(\cdot, t) = v_D\,\xi(t) \cdot e_1$ prescribes a smooth transition from zero velocity to constant loading speed $v_D = 2 \times 10^{-4}$m/s with

$$\xi(t) = \begin{cases} \frac{1}{2}(1 - \cos(4\pi t/T_0)), & \text{if } t \leq T_0/10 \\ 1 & \text{otherwise.} \end{cases} \tag{60}$$

At the interfaces, $\Gamma^F = \bigcup_{i=1}^{I-1} \Gamma_{i,i+1}^F$ we impose rate-and-state friction conditions with Dieterich's aging law.

The initial deformation $u(\cdot, 0)$ is obtained by approximating the equilibrium configuration, i.e., the solution of the stationary problem Eq. 35, by one step of the associated fixed point iteration. The initial velocity field is set to zero, which is consistent with the Dirichlet conditions, and the initial state field is chosen to be $\alpha(\cdot, 0) = -10$ on Γ^F.

We consider the time interval $[0, T_0]$ with final time $T_0 = 60$s, and the remaining material parameters are given in Table 1.

6.1.2 Discretization and algebraic solution

In order to efficiently resolve strongly varying dynamics ranging from slow interseismic loading to fast coseismic periods, corresponding time step sizes are automatically selected according to the following adaptive strategy. For given approximate solution at t_n of the coupled spatial Problem 3 at time $t_n \in [0, T_0)$, as computed by the old time step size τ_{n-1}, we choose $\tau_n^* = \tau_{n-1}$ for $n \geq 1$ and $\tau_{-1} = 10^{-4}\,T_0$ as an initial guess for the new time step size τ_n. Then, we compute approximate solutions $(\dot{u}_{n+1}^{(1)}, \alpha_{n+1}^{(1)})$ at $t_n + 2\tau_n^*$ by one step with step size $2\tau_n^*$ and $(\dot{u}_{n+1}^{(2)}, \alpha_{n+1}^{(2)})$ by two time steps with step size τ_n^*. If the criterion

$$\|\alpha_{n+1}^{(1)} - \alpha_{n+1}^{(2)}\|_{L^2(\Gamma^F)} \leq \delta_\tau \text{ m}^{1/2} \tag{61}$$

holds with a suitable threshold δ_τ, then we allow for coarsening: With the new guess $\tau_n^* := 2\tau_n^*$ the above procedure is repeated until Eq. 61 is violated and we set $\tau_n := \tau_n^*/2$ in this case. If the criterion Eq. 61 is already violated by the initial guess $\tau_n^* = \tau_{n-1}$, then we require refinement: Successive bisection $\tau_n^* := \tau_n^*/2$ is applied until Eq. 61 is met and we set $\tau_n := \tau_n^*$ in this case. The threshold δ_τ is selected in accordance with the accuracy of the inner fixed point iteration to be specified below.

The spatial problems occurring in each time step are discretized with respect to triangulations $\mathcal{T}_i = \mathcal{T}_i^{(K)}$, as resulting from K refinement steps applied to initial triangulations $\mathcal{T}_i^{(0)}$ of the subdomains $\Omega_i, i = 1, \dots, I$. Note that the associated

Table 1 Material parameters

Bulk parameter	Value	Friction parameter	Value
Bulk modulus E	4.12×10^7 Pa	ref. velocity V_0	1×10^{-6}m/s
Poisson ratio ν	0.3	ref. friction coeff. μ_0	0.6
mass density ρ	5×10^3kg/m^2	a	0.010
gravity g	9.81 N/kg	b	0.015
		charact. slip dist. L	1×10^{-5}m

hierarchy of finite element spaces is utilized for the algebraic TNNMG solver to be specified later on. For the spring slider and the layered fault system, the initial triangulations $\mathcal{T}_i^{(0)}$, $i = 1, \ldots, I$, are shown in the left and in the right picture of Fig. 2, respectively.

For both geometries, refinement is concentrated at the interfaces by the following adaptive procedure. Starting with $\mathcal{T}_i^{(0)}$, we perform regular (red) refinement of all triangles $T \in \mathcal{T}_i^{(k)}$, $k \geq 0$, with diameter h_T violating the criterion

$$h_T < (1 + 80\, d(T, \Gamma^F))\, h_{\min}. \tag{62}$$

Here, $d(T, \Gamma^F)$ stands for the distance of T to Γ^F and $h_{\min} = 6.25\,\text{cm}$. Then, triangles with two or three bisected edges as emerging through this procedure are also refined regularly until only triangles with no or with only one bisected edge are left from $\mathcal{T}^{(k)}$. The latter ones are then refined by connecting the midpoint of this edge with the opposite vertex to obtain conforming refined triangulations $\mathcal{T}_i^{(k+1)}$. In order to preserve shape regularity, these (green) closures are removed in advance of the next refinement step [2]. Refinement terminates with $K = k$, once the criterion Eq. 62 is met by all triangles $T \in \mathcal{T}_i^{(k)}$ and all $i = 1, \ldots, I$.

The resulting final triangulations are depicted in Fig. 3. For the spring slider (left), the final triangulations $\mathcal{T}_i^{(K)}$ are resulting from $K = 5$ adaptive refinement steps, have 1274 vertices in total, and $4.4\,\text{cm} \leq h_T \leq 70.8\,\text{cm}$ holds for the diameters h_T of all $T \in \mathcal{T}_i^{(K)}$, $i = 1, 2$. For the layered fault system (right), the final triangulations $\mathcal{T}_i^{(K)}$ are obtained after $K = 5$ refinement steps, have 4057 vertices in total, and $3.2\,\text{cm} \leq h_T \leq 70.8\,\text{cm}$ holds for the diameters h_T of all $T \in \mathcal{T}_i^{(K)}$, $i = 1, \ldots, 5$.

In the fixed point iteration Eq. 53, providing the decoupling of rate and state, we use the relaxation parameter $\omega = 1/2$. The iteration is stopped, once the criterion

$$\|\alpha_{n,\mathcal{B}}^{\nu} - \alpha_{n,\mathcal{B}}^{\nu-1}\|_{L^2(\Gamma^F)} \leq 10^{-1}\delta_\tau\ \text{m}^{1/2} \tag{63}$$

is satisfied. Here, the parameter δ_τ is the same as in the time step selection criterion Eq. 61. This choice aims at comparable accuracy of fixed point iteration and time stepping, and the actual value $\delta_\tau = 10^{-5}$ is motivated by systematic trial and error, cf. [32][Subsection 3.3].

The algebraic solution of the discrete state problem Eq. 43 with Dieterich's aging law and given rate is approximated by pointwise bisection. The iteration is stopped, once the error in each node is uniformly bounded by the threshold $10^{-12}\text{m}^{1/2}$.

Starting with the final iterate $\dot{u}_{n,\mathcal{S}}^0 = \dot{u}_{n-1,\mathcal{S}}^{\nu_{\text{stop}}}$ from the preceding time step, the algebraic solution of the discrete rate problem Eq. 50 with given state is performed by a Truncated Nonsmooth Newton Multigrid (TNNMG) method as described in Section 5.2. In each iteration step, the (truncated) linear correction is obtained by 5 steps of a classical multigrid V-cycle with 3 pre- and 3 post-smoothing steps. Here, we utilize the grid hierarchy provided by successive refinement described above. The iteration is terminated, once the stopping criterion

$$\|\dot{u}^{\nu} - \dot{u}^{\nu-1}\|_n \leq 10^{-8}\text{W}^{1/2}\text{m}^{1/2} \tag{64}$$

is satisfied with the time-dependent energy norm $\|\cdot\|_n = a_n(\cdot,\cdot)^{1/2}$ and $a_n(\cdot,\cdot)$ defined in Eq. 39. This stopping criterion is selected to reduce the error of the inner multigrid iteration some orders of magnitude below the error of the outer fixed point iteration which is intended to be in the range of the discretization error.

The discretization and algorithms are implemented using the Dune framework [4] making use of the dune-grid-glue library [5] for the mortar coupling.

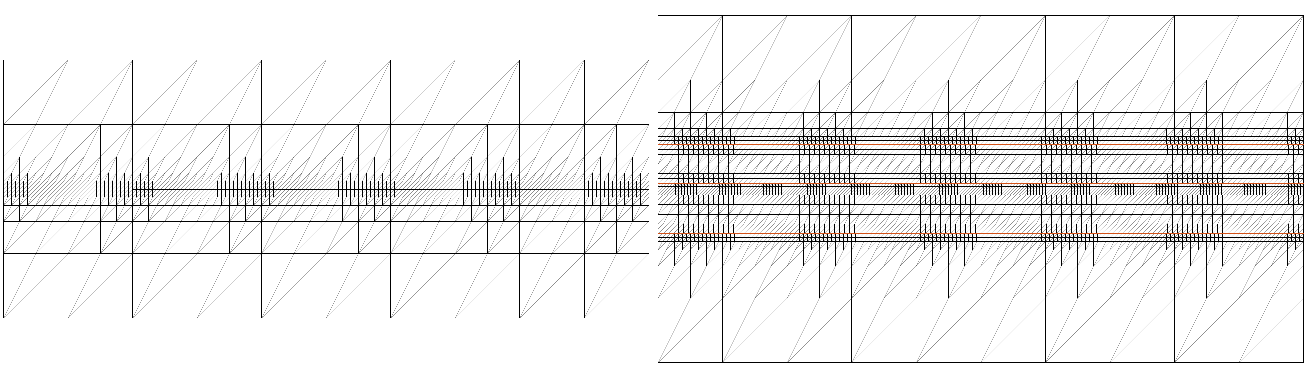

Fig. 3 Adaptively refined final triangulations $T \in \mathcal{T}_i^{(K)}$, $i = 1, \ldots, I$ with $K = 5$ and 1274 vertices for the spring slider (left) and $K = 5$ and 4057 vertices for the layered fault system (right)

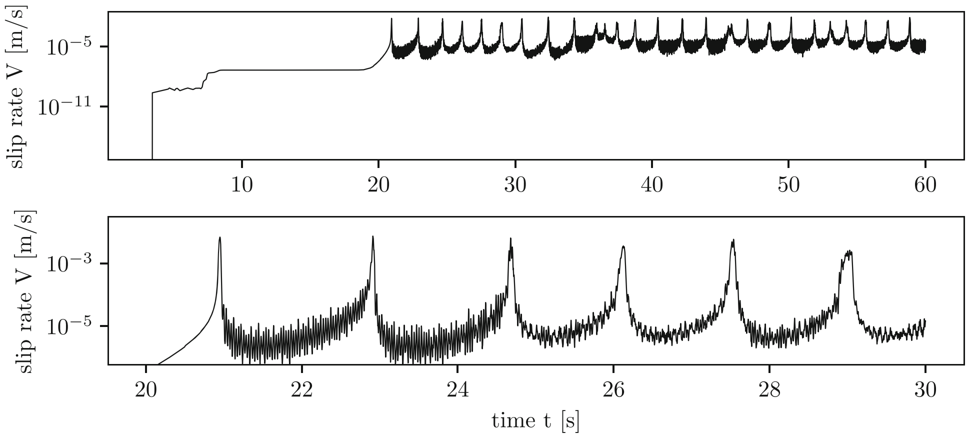

Fig. 4 Spring slider: Evolution of the mean value of relative velocities over Γ^F from the initial loading phase to slip events (top) and zoom into the slip events (bottom)

6.2 Spring slider

6.2.1 Simulation results

In order to illustrate the behavior of the deformed bodies along the fault $\Gamma^F = (-2.5, 2.5) \times \{0\}$, the top picture of Fig. 4 shows the mean value of the approximate relative velocitiy $|\,[\dot{u}_{n,\mathcal{S}}]^{u_{n-1,\mathcal{S}}}|$ over Γ^F for the corresponding time instants t_n, $n = 1, \ldots, N = 107659$. After a loading phase of about 20s, we observe 26 almost periodic peaks in the relative velocity, indicating the occurrence of corresponding slip events. Observe that periodicity is slightly perturbed in comparison with related numerical results for a rigid foundation [33]. A zoom into the first 6 slip events as shown in the bottom picture of Fig. 4 reveals a highly oscillatory behavior of the approximate velocity. This is partly due to the well-known lack of stability of the Newmark scheme [23], but also occurs for the highly dissipative backward Euler method [34] and sufficiently fine time steps.

Figure 5 shows the level lines of approximate relative velocities along the fault Γ^F (horizontal axis) evolving over time (vertical axis) for six time intervals associated with

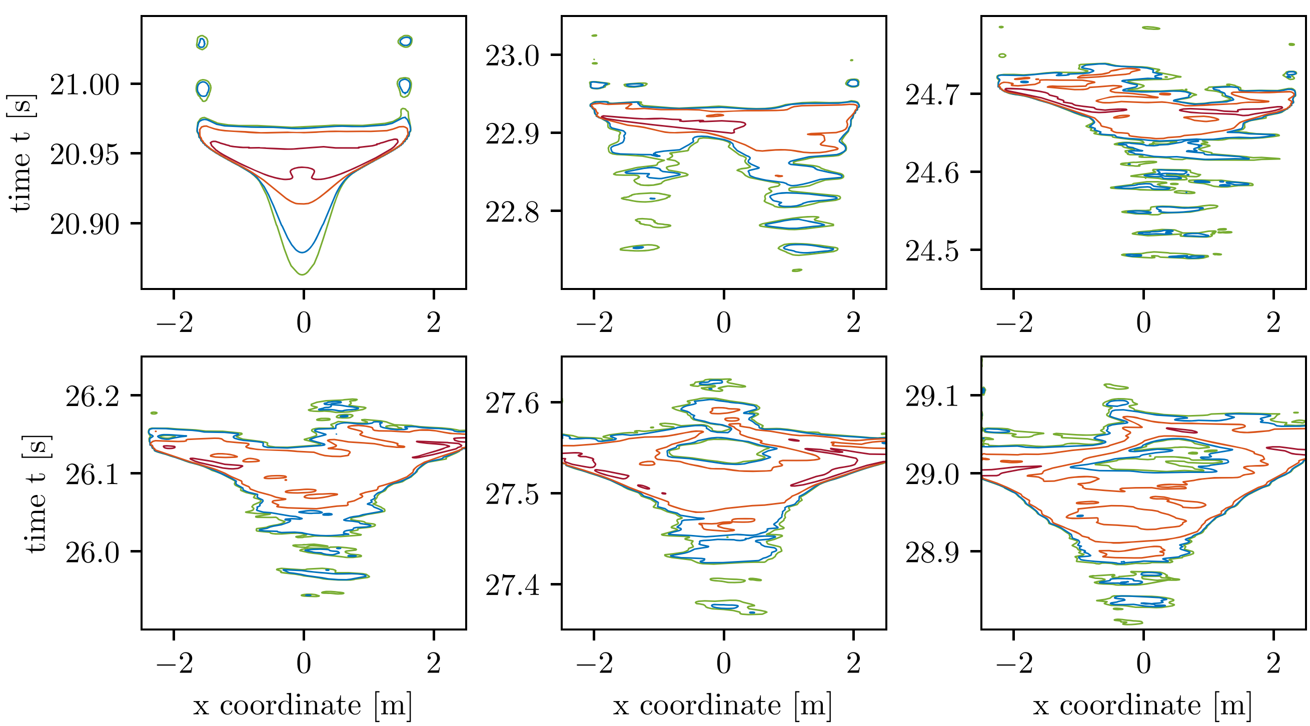

Fig. 5 Spring slider: Level lines (10^1 µm/s green, 10^2 µm/s blue, 10^3 µm/s orange, 10^4 µm/s red) of the approximate relative velocity along Γ^F over time intervals associated with the first 6 slip events

the first six slip events (top left to bottom right). The first (bilateral) slip event originates from the midpoint of Γ^F, the next one has two symmetric precursors on the left and right hand side, and the third one features foreshocks with a slight emphasis towards the right hand side of Γ^F, but ruptures the entire fault nonetheless. We then observe a sequence of three further bilateral slip events beginning in the middle of the fault.

All slip events are preceded by small foreshocks indicating the origin of the later event, as well as small aftershocks typically occurring at the right or left side of Γ^F or in its very center. Note that these results considerably differ from related computations for a subduction zone with rigid foundation that showed pure periodic behavior [32].

6.2.2 Adaptive time stepping and performance of the algebraic solver

We now describe the performance of adaptive time step selection and of the algebraic solver consisting of the fixed point iteration Eq. 53 for the decoupling of rate and state and the TNNMG method for the rate problem as explained in Section 5.2. The upper picture of Fig. 6 shows the automatically selected time step sizes τ_n over corresponding time instants t_n taken from the time interval that begins shortly before the end of the initial loading phase. Observe that the occurrence of slip events is nicely reflected by the reduction of the time step size by about 2 orders of magnitude. According to the second picture, usually 2 - 4 fixed point iterations are required to match the stopping criterion Eq. 63 for the actual spatial problem with adaptively selected time step. The third picture shows the sum of all inner multigrid iterations as needed to reach the stopping criterion Eq. 64 in each of these outer fixed point iteration steps. This sum often, but not always, increases and decreases with the number of required outer fixed point iterations and is ranging from about 5 to 29.

6.3 Layered fault system

6.3.1 Simulation results

Figure 7 indicates quite interesting stress accumulation and release along the different faults. The four pictures show the mean value of the relative velocity on the faults $\Gamma^F_{4,5}$, $\Gamma^F_{3,4}$, $\Gamma^F_{2,3}$, and $\Gamma^F_{1,2}$ (top to bottom) over time. In the first picture for the upper fault $\Gamma^F_{4,5}$, we observe a sequence of almost periodic slip events with almost the same period and amplitude as for the spring slider, again after an initial loading phase of about 26 s. In both of the next two pictures, however, showing the average relative velocities over the next two faults $\Gamma^F_{3,4}$ and $\Gamma^F_{2,3}$, we see a highly oscillatory loading phase that seems to depict slip events several orders of magnitude smaller than on the top fault $\Gamma^F_{4,5}$ and might have saturated after a small jump at about 47 s or lead to later slip events. It is not clear at the moment whether the occurance and amplitude of these oscillations are physical or due to numerical artifacts which would motivate future numerical and experimental investigations. As shown in the fourth picture, this jump of average relative velocity also occurs at the lowest fault $\Gamma^F_{1,2}$, this time preceded by a rather stable loading phase.

Figure 8 shows the level lines of approximate relative velocities along the upper fault $\Gamma^F_{4,5}$ (horizontal axis) evolving over six time intervals (vertical axis) associated with the first six slip events (top left to bottom right). All events exhibit bilateral characteristics, i.e. ruptures nucleating towards the center of the fault and spreading towards both edges, preceded by small foreshocks occurring in the middle of $\Gamma^F_{4,5}$. In most (but not all) cases the slip events are followed by small aftershocks. These observations are in strong analogy

Fig. 6 Spring slider: Adaptive time step selection and performance of the algebraic solver

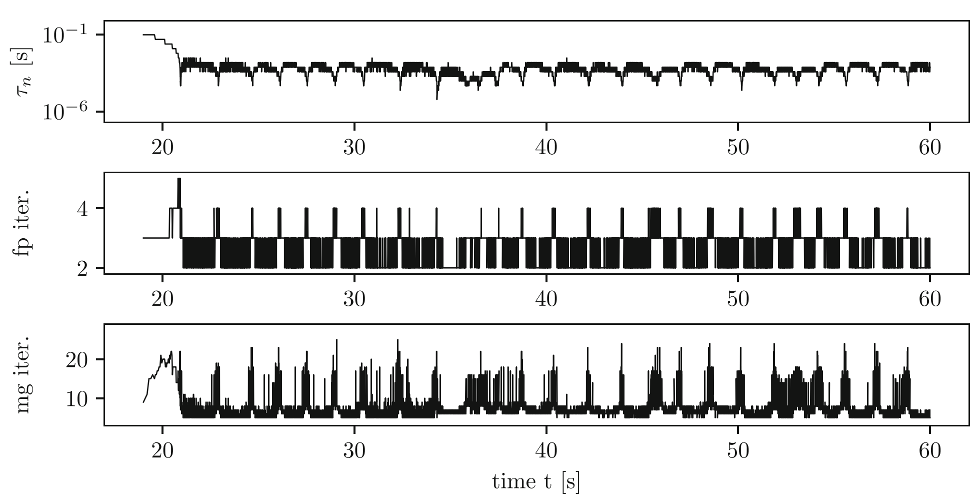

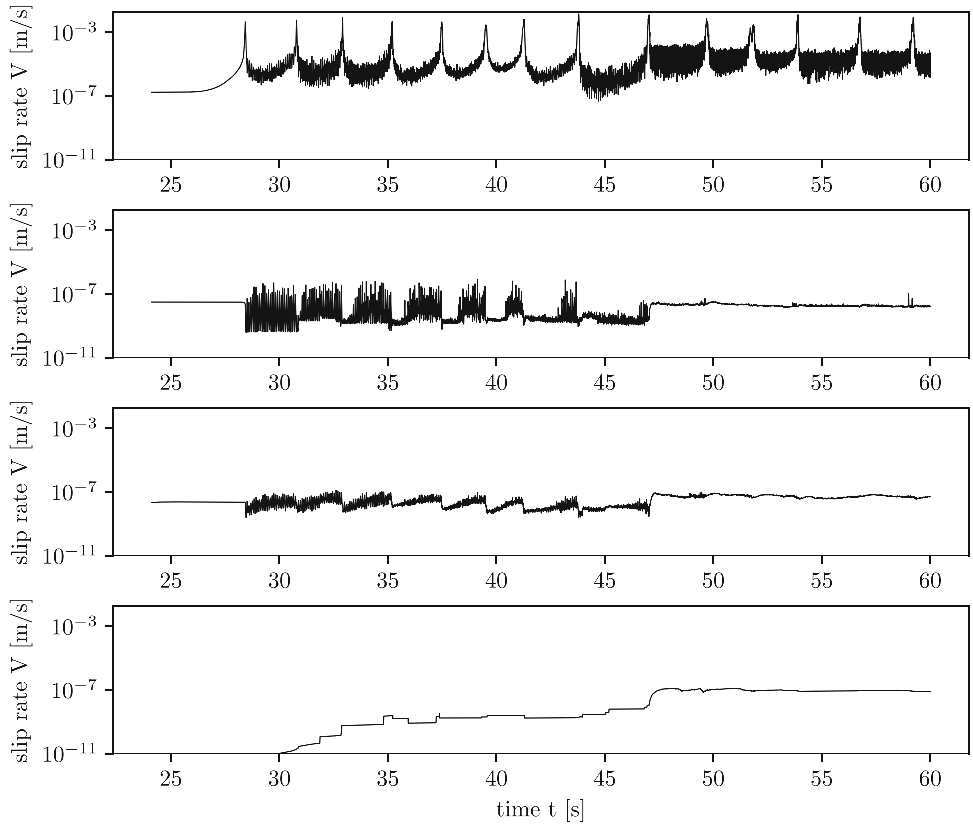

Fig. 7 Layered fault system: Evolution of the mean value of relative velocities over the faults $\Gamma^F_{i,i+1}$, $i = 1, 2, 3, 4$, from $\Gamma^F_{4,5}$ (top) to $\Gamma^F_{1,2}$ (bottom)

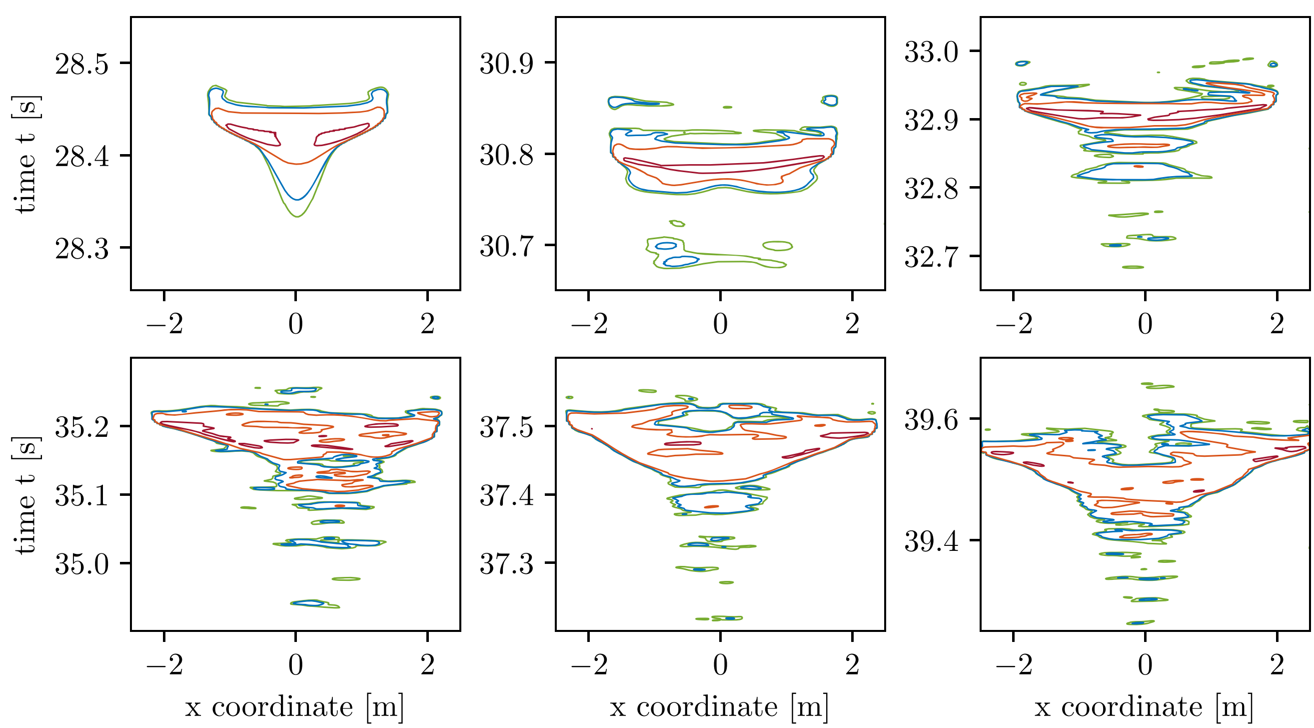

Fig. 8 Layered fault system: Level lines ($10^1\,\mu$m/s green, $10^2\,\mu$m/s blue, $10^3\,\mu$m/s orange, $10^4\,\mu$m/s red) of the approximate relative velocity along Γ^F_{34} over time intervals associated with the first 6 slip events

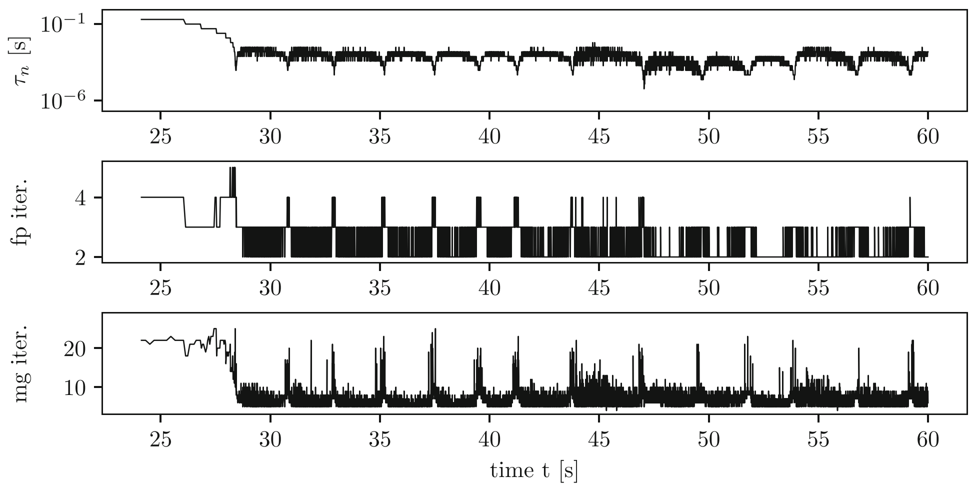

Fig. 9 Layered fault system: Adaptive time step selection and performance of the algebraic solver

with the results of the spring slider experiment as depicted in Fig. 5.

6.3.2 Adaptive time step selection and performance of the algebraic solver

The performance of adaptive time step selection and of the algebraic solver as illustrated in Fig. 9 hardly differs from the spring slider experiment. Again, the slip events on $\Gamma^F_{4,5}$ are well-captured by adaptive time stepping that is reducing the time step by about 2 orders of magnitude. The number of outer fixed point iterations still ranges from 2 to 4 and the sum of all inner multigrid iterations in each of these steps is bounded by 25, apart from slightly larger values at the end of the loading phase. This strongly confirms the efficiency and robustness of our solution approach.

7 Conclusions

In the present paper we showed how the variational approach to problems with rate- and state-dependent friction introduced in [32] can be generalized to layered fault systems. By combining a linearized strain rate tensor and large deformation contact conditions, the variational model allows for small viscoelastic deformations within and large relative displacements between layers. The considered variational friction model includes Dieterich- and Ruina-type friction.

Thanks to the variational structure of the model, the proposed discretization using a Newmark scheme and a mortar finite element ansatz leads to a sequence of discrete coupled minimization problems, that can be decoupled using a fixed point method. Despite beeing nonlinear and nonsmooth the resulting sequence of minimization problems can be solved efficently by combining a dual mortar ansatz with the Truncated Nonsmooth Newton Multigrid method.

In the presented numerical experiments for a spring slider problem we observed the periodic occurrence of mostly unilateral slip events. For the numerical experiments for a layered network we observed an interesting coincidence of periodic slip events along the upper fault with loading phases and oscillatory behavior on the others. For both types of experiments slip events are captured nicely by an adaptive time stepping scheme, while the computational complexity in each time step remains bounded. This illustrates the robustness of the presented numerical solution procedure, also with respect to the number of faults.

In view of the observed robusteness and efficiency the presented approach looks promissing for the application in more complicated application settings to be considered in future work.

Funding Open Access funding enabled and organized by Projekt DEAL. This research has been funded by Deutsche Forschungsgemeinschaft (DFG) through grant CRC 1114 “Scaling Cascades in Complex Systems”, Project Number 235221301, Project B01 “Fault networks and scaling properties of deformation accumulation”

Data Availability The datasets generated during and/or analysed during the current study are available from the corresponding author on reasonable request

Declarations

Competing interests The authors have no competing interests to declare that are relevant to the content of this article

References

1. Ampuero, J.P., Rubin, A.: Earthquake nucleation on rate and state faults - aging and slip laws. J. Geophys. Res. **113**(B1), B01302 (2008)
2. Bank, R.E., Sherman, A.H., Weiser, A.: Some refinement algorithms and data structures for regular local mesh refinement. Sci. Comput. Appl. Math. Comput. Phys. Sci. **1**, 3–17 (1983)
3. Barbot, S., Lapusta, N., Avouac, J.-P.: Under the hood of the earthquake machine: Toward predictive modeling of the seismic cycle. Science **336**(6082), 707–710 (2012)
4. Bastian, P., Blatt, M., Dedner, A., Dreier, N.-A., Engwer, C., Fritze, R., Gräser, C., Grüninger, C., Kempf, D., Klöfkorn, R., Ohlberger, M., Sander, O.: The DUNE framework: Basic concepts and recent developments. Comput. Math, Appl (2020)
5. Bastian, P., Buse, G., Sander, O.: Infrastructure for the coupling of Dune grids. In Numerical Mathematics and Advanced Applications 2009, pp 107–114. Springer, (2010)
6. Beeler, N.M., Tullis, T.E., Weeks, J.D.: The roles of time and displacement in the evolution effect in rock friction. Geophys. Res. Lett. **21**(18), 1987–1990 (1994)
7. Ben-Zion, Y.: Collective behavior of earthquakes and faults: Continuum-discrete transitions, progressive evolutionary changes, and different dynamic regimes. Reviews Geophys. 46(4) (2008)
8. Cochard, A., Madariaga, R.: Dynamic faulting under rate-dependent friction. Pure Appl. Geophys. **142**(3), 419–445 (1994)
9. Dal Zilio, L., van Dinther, Y., Gerya, T.V., Pranger, C.C.: Seismic behaviour of mountain belts controlled by plate convergence rate. Earth Planetary Sci. Lett. **482**, 81–92 (2018)
10. de la Puente, J., Ampuero, J.-P., Käser, M.: Dynamic rupture modeling on unstructured meshes using a discontinuous Galerkin method. J. Geophys. Res. Solid Earth 114(B10) (2009)
11. Fagereng, A., Toy, V.: Geology of the earthquake source: an introduction. Geological Soc. London Special Pub. **359**(1), 1–16 (2011)
12. Fonseca, I., Leoni, G.: Modern Methods in the Calculus of Variations: Lˆp Spaces. Springer Science & Business Media, (2007)
13. Glowinski, R.: Numerical methods for non-linear variational problems. Springer Verlag, (1984)
14. Gräser, C.: Convex Minimization and Phase Field Models. PhD thesis, Freie Universität Berlin, (2011)
15. Gräser, C., Sack, U., Sander, O.: Truncated nonsmooth Newton multigrid methods for convex minimization problems. In Bercovier, M., Gander, M., Kornhuber, R., Widlund, O. (Eds.) Domain Decomposition Methods in Science and Engineering XVIII, vol 70 of LNCSE, pp 129–136 Springer, (2009)
16. Gräser, C., Sander, O.: Truncated nonsmooth Newton multigrid methods for block-separable minimization problems. IMA J. Numer. Anal. **39**, 454–481 (2019)
17. Hairer, E., Lubich, C., Wanner, G.: Geometric Numerical Integration: Structure-Preserving Algorithms for Ordinary Differential Equations, vol. 31, 2nd edn. Springer-Verlag, Berlin Heidelberg (2006)
18. Heinecke, A., Breuer, A., Rettenberger, S., Bader, M., Gabriel, A.-A., Pelties, C., Bode, A., Barth, W., Liao, X.-K., Vaidyanathan, K., et al.: Petascale high order dynamic rupture earthquake simulations on heterogeneous supercomputers. SC'14: Proceedings of the International Conference for High Performance Computing, Networking, Storage and Analysis, pp 3–14. IEEE, (2014)
19. Herrendörfer, R., Van Dinther, Y., Gerya, T., Dalguer, L.A.: Earthquake supercycle in subduction zones controlled by the width of the seismogenic zone. Nature Geosci. **8**(6), 471–474 (2015)
20. Kačur, J.: Method of Rothe in evolution equations. In Equadiff 6, pp 23–34. Springer, (1986)
21. Kato, N.: Interaction of slip on asperities: Numerical simulation of seismic cycles on a two-dimensional planar fault with nonuniform frictional property. J. Geophys. Res. Solid Earth 109(B12) (2004)
22. Krause, R.H.: A nonsmooth multiscale method for solving frictional two-body contact problems in 2d and 3d with multigrid efficiency. SIAM J. Sci. Comput. **31**(2), 1399–1423 (2009)
23. Krause, R.H., Walloth, M.: Presentation and comparison of selected algorithms for dynamic contact based on the Newmark scheme. Appl. Num. Math. **62**(10), 1393–1410 (2012)
24. Krause, R.H., Wohlmuth, B.I.: A Dirichlet-Neumann type algorithm for contact problems with friction. Comput. Vis. Sci. **5**(3), 139–148 (2002)
25. Lapusta, N., Rice, J.R., Ben-Zion, Y., Zheng, G.: Elastodynamic analysis for slow tectonic loading with spontaneous rupture episodes on faults with rate-and state-dependent friction. J. Geophys. Res. Solid Earth **105**(B10), 23765–23789 (2000)
26. Madden, E.H., Bader, M., Behrens, J., van Dinther, Y., Gabriel, A.-A., Rannabauer, L., Ulrich, T., Uphoff, C., Vater, S., Wollherr, S.: Methods and test cases for linking physics-based earthquake and tsunami models. (2019)
27. Marone, C.: Laboratory-derived friction laws and their application to seismic faulting. Annual Rev. Earth Planetary Sci. **26**(1), 643–696 (1998)
28. Meister, O., Rahnema, K., Bader, M.: Parallel memory-efficient adaptive mesh refinement on structured triangular meshes with billions of grid cells. ACM Trans. Math. Softw. (TOMS) **43**(3), 1–27 (2016)
29. Pelties, C., De la Puente, J., Ampuero, J.-P., Brietzke, G. B., Käser, M.: Three-dimensional dynamic rupture simulation with a high-order discontinuous Galerkin method on unstructured tetrahedral meshes. J. Geophys. Res. Solid Earth 117(B2) (2012)
30. Pipping, E.: Dynamic problems of rate- and state friction in viscoelasticity. PhD thesis, Freie Universität Berlin, (2014)
31. Pipping, E.: Existence of long-time solutions to dynamic problems of viscoelasticity with rate-and-state friction. ZAMM-J. Appl. Math. Mechanics/Zeitschrift für Angewandte Mathematik und Mechanik 99(11), e201800263 (2019)
32. Pipping, E., Kornhuber, R., Rosenau, M., Oncken, O.: On the efficient and reliable numerical solution of rate-and-state friction problems. Geophys. J. Int. **204**(3), 1858–1866 (2016)
33. Pipping, E., Sander, O., Kornhuber, R.: Variational formulation of rate- and state-dependent friction problems. ZAMM - J. Appl. Math. Mech./Zeitschrift für Angewandte Mathematik und Mechanik, 95(4), 377–395 (2015)
34. Podlesny, J.: Multiscale Modelling and Simulation of Deformation Accumulation in Fault Networks. PHD thesis, Freie Universität Berlin, (2021)
35. Ranjith, K., Rice, J.R.: Stability of quasi-static slip in a single degree of freedom elastic system with rate and state dependent friction. J. Mech. Phys. Solids **47**(6), 1207–1218 (1999)
36. Rice, J.R., Ben-Zion, Y.: Slip complexity in earthquake fault models. Proceed. National Acad. Sci. **93**(9), 3811–3818 (1996)
37. Rice, J.R., Lapusta, N., Ranjith, K.: Rate and state dependent friction and the stability of sliding between elastically deformable solids. J. Mech. Phys. Solids **49**(9), 1865–1898 (2001)
38. Rosenau, M., Lohrmann, J., Oncken, O.: Shocks in a box: An analogue model of subduction earthquake cycles with application to seismotectonic forearc evolution. J. Geophys. Res. Solid Earth 114(B1) (2009)

39. Rothe, E.: Zweidimensionale parabolische Randwertaufgaben als Grenzfall eindimensionaler Randwertaufgaben. Math. Annalen **102**(1), 650–670 (1930)
40. Ruina, A.: Slip instability and state variable friction laws. J. Geophys. Res. **88**(B12), 10359–10370 (1983)
41. Sander, O.: Multidimensional Coupling in a Human Knee Model. PhD thesis, Freie Universität Berlin, (2008)
42. Sander, O.: The PSurface library. Comp. Vis. Sci. **14**(8), 353–370 (2011)
43. Scholz, C.: Earthquakes and friction laws. Nature **391**(6662), 37–42 (1998)
44. Sobolev, S.V., Muldashev, I.A.: Modeling seismic cycles of great megathrust earthquakes across the scales with focus at postseismic phase. Geochem. Geophys. Geosyst. **18**(12), 4387–4408 (2017)
45. Ulrich, T., Gabriel, A.-A., Ampuero, J.-P., Xu, W.: Dynamic viability of the 2016 mw 7.8 Kaikōura earthquake cascade on weak crustal faults. Nature Commun. **10**(1), 1–16 (2019)
46. Van Dinther, Y., Gerya, T.V., Dalguer, L.A., Mai, P.M., Morra, G., Giardini, D.: The seismic cycle at subduction thrusts: Insights from seismo-thermo-mechanical models. J. Geophys. Res. Solid Earth **118**(12), 6183–6202 (2013)
47. Wohlmuth, B.I.: A mortar finite element method using dual spaces for the Lagrange multiplier. SIAM J. Num. Anal. **38**(3), 989–1012 (2000)
48. Wohlmuth, B.I.: Variationally consistent discretization schemes and numerical algorithms for contact problems. Acta Numerica **20**, 569–734 (2011)
49. Wohlmuth, B.I., Krause, R.H.: Monotone multigrid methods on nonmatching grids for nonlinear multibody contact problems. SIAM J. Sci. Comput. **25**(1), 324–347 (2003)